



UPPSALA  
UNIVERSITET

*Digital Comprehensive Summaries of Uppsala Dissertations  
from the Faculty of Science and Technology 1673*

# Plasma and Dust around Icy Moon Enceladus and Comet 67P/ Churyumov-Gerasimenko

ILKA. A. D. ENGELHARDT



ACTA  
UNIVERSITATIS  
UPSALIENSIS  
UPPSALA  
2018

ISSN 1651-6214  
ISBN 978-91-513-0346-8  
urn:nbn:se:uu:diva-348856

Dissertation presented at Uppsala University to be publicly examined in 2001, Ångströmlaboratoriet, Lägerhyddsvägen 1, Uppsala, Monday, 11 June 2018 at 13:00 for the degree of Doctor of Philosophy. The examination will be conducted in English. Faculty examiner: Professor Ingrid Mann (The Arctic University of Norway, Department of Physics and Technology, Tromsø, Norway).

### Abstract

Engelhardt, I. A. D. 2018. Plasma and Dust around Icy Moon Enceladus and Comet 67P/Churyumov-Gerasimenko. *Digital Comprehensive Summaries of Uppsala Dissertations from the Faculty of Science and Technology* 1673. 94 pp. Uppsala: Acta Universitatis Upsaliensis. ISBN 978-91-513-0346-8.

Saturn's moon Enceladus and comet 67P/Churyumov-Gerasimenko both are examples of icy solar system objects from which gas and dust flow into space. At both bodies, the gas becomes partly ionized and the dust grains get charged. Both bodies have been visited by spacecraft carrying similar Langmuir probe instruments for observing the plasma and the charged dust. As it turns out, the conditions at Enceladus and the comet are different and we emphasize different aspects of their plasma environments. At Enceladus, we concentrate on the characteristic plasma regions and charged dust. At the comet, we investigate the plasma and in particular plasmavariations and cold electrons.

At Enceladus, internal frictional heating leads to gas escaping from cracks in the ice from the south pole region. This causes a plume of gas, which becomes partially ionized, and dust, becoming charged. We have investigated the plasma and charged nanodust in this region by the use of the Langmuir probe (LP) of the Radio and Plasma Wave Science (RPWS) instrument on Cassini. The dust charge density can be calculated from the quasineutrality condition, the difference between ion and electron density measurements from LP. We found support for this method by comparing to measurements of larger dust grains by the RPWS electric antennas. We use the LP method to find that the plasma and dust environment of Enceladus can be divided into at least three regions. In addition to the well known plume, these are the plume edge and the trail region.

At the comet, heat from the Sun sublimates ice to gas dragging dust along as it flows out into space. When the neutral gas molecules are ionized, by photoionization and electron impact ionization, we get a plasma. Models predict that the electron temperature just after ionization is around 10 eV, but that collisions with the neutral gas should cool the electron gas to below 0.1 eV. We used the Langmuir probe instrument (LAP) on Rosetta to estimate plasma temperatures and show a co-existence of cold and warm electrons in the plasma. We find that the cold plasma often is observed as brief pulses not only in the LAP data but also in the measurements of magnetic field, plasma density and ion energy by other Rosetta plasma instruments. We interpret these pulses as filaments of plasma propagating outwards from a diamagnetic cavity, as predicted by hybrid simulations. The gas production rate of comet 67P varied by more than three orders of magnitude during the Rosetta mission (up to March 2016). We therefore have an excellent opportunity to investigate how the electron cooling in a cometary coma evolves with activity. We used a method combining LAP and the Mutual Impedance Probe (MIP) for deriving the presence of cold electrons. We show that cold electrons were present intermittently during a large part of the mission and as far out as 3 AU. Models suggest only negligible cooling and we suggest that the ambipolar field keeps the electrons close to the nucleus and giving them more time to lose energy by collision.

*Ilka. A. D. Engelhardt, Department of Physics and Astronomy, Space Plasma Physics, 516, Uppsala University, SE-751 20 Uppsala, Sweden.*

© Ilka. A. D. Engelhardt 2018

ISSN 1651-6214

ISBN 978-91-513-0346-8

urn:nbn:se:uu:diva-348856 (<http://urn.kb.se/resolve?urn=urn:nbn:se:uu:diva-348856>)

To my parents,  
Dorothée and Ralph



# Foreword

## Thesis

This PhD thesis is partly based on “Plasma and Dust at Saturn’s Icy Moon Enceladus and Comet 67P/Churyumov-Gerasimenko,” Licentiate dissertation, Uppsala University, 2016, by I.A.D. Engelhardt. Chapters 1 to 7 and chapter 9 were reused and modified. Other chapters are new.

## Thesis Layout

The thesis layout is based on the "Legrand Orange Book"

<https://www.latextemplates.com/template/the-legrand-orange-book>

## Thesis Cover

The pictures for the front and back cover are a compilation of the following pictures:

**Front** <https://photojournal.jpl.nasa.gov/catalog/PIA21338>

[http://www.esa.int/spaceinimages/Images/2015/07/Comet\\_on\\_7\\_July\\_2015\\_NavCam](http://www.esa.int/spaceinimages/Images/2015/07/Comet_on_7_July_2015_NavCam)

**Back** <https://photojournal.jpl.nasa.gov/catalog/PIA08321>

[http://www.esa.int/spaceinimages/Images/2015/10/Comet\\_on\\_30\\_September\\_2015\\_NavCam](http://www.esa.int/spaceinimages/Images/2015/10/Comet_on_30_September_2015_NavCam)

## Source for Heading Pictures

In the following list the link to the picture is given for each chapter.

### Table of Contents

<https://photojournal.jpl.nasa.gov/jpeg/PIA11800.jpg>

### Chapter 1

<https://photojournal.jpl.nasa.gov/catalog/PIA03654>

### Chapter 2

[https://www.nasa.gov/images/content/402561main\\_cassini20091113-full.jpg](https://www.nasa.gov/images/content/402561main_cassini20091113-full.jpg)

### Chapter 3

<https://history.nasa.gov/EP-177/i2-31.jpg>

### Chapter 4

<https://www.jpl.nasa.gov/missions/web/cassini.jpg>

### Chapter 5

<https://www.jpl.nasa.gov/images/cassini/20151028/enceladus-16.jpg>

### Chapter 6

[http://www.esa.int/var/esa/storage/images/esa\\_multimedia/images/2007/03/enceladus\\_ice\\_jets\\_send\\_particles\\_streaming\\_into\\_space/9239372-5-eng-GB/Enceladus\\_ice\\_jets\\_send\\_particles\\_streaming\\_into\\_space.jpg](http://www.esa.int/var/esa/storage/images/esa_multimedia/images/2007/03/enceladus_ice_jets_send_particles_streaming_into_space/9239372-5-eng-GB/Enceladus_ice_jets_send_particles_streaming_into_space.jpg)

### Chapter 7

[http://www.esa.int/var/esa/storage/images/esa\\_multimedia/images/2014/10/rosetta\\_mission\\_selfie\\_at\\_16\\_km/14968938-1-eng-GB/Rosetta\\_mission\\_selfie\\_at\\_16\\_km.png](http://www.esa.int/var/esa/storage/images/esa_multimedia/images/2014/10/rosetta_mission_selfie_at_16_km/14968938-1-eng-GB/Rosetta_mission_selfie_at_16_km.png)

### Chapter 8

[https://upload.wikimedia.org/wikipedia/commons/thumb/2/2a/Lspn\\_comet\\_halley.jpg/1280px-Lspn\\_comet\\_halley.jpg](https://upload.wikimedia.org/wikipedia/commons/thumb/2/2a/Lspn_comet_halley.jpg/1280px-Lspn_comet_halley.jpg)

### Chapter 12

<https://photojournal.jpl.nasa.gov/catalog/PIA06254>  
and  
[http://www.esa.int/spaceinimages/Images/2014/08/Comet\\_on\\_3\\_August\\_2014](http://www.esa.int/spaceinimages/Images/2014/08/Comet_on_3_August_2014)

### Bibliography

[https://upload.wikimedia.org/wikipedia/commons/thumb/8/87/Old\\_book\\_bindings.jpg/1024px-Old\\_book\\_bindings.jpg](https://upload.wikimedia.org/wikipedia/commons/thumb/8/87/Old_book_bindings.jpg/1024px-Old_book_bindings.jpg)

### Acronyms

<http://www.wordle.net>

### Swedish Summary

[https://commons.wikimedia.org/wiki/File:Swedish\\_flag.jpg](https://commons.wikimedia.org/wiki/File:Swedish_flag.jpg)

## List of Articles

This thesis is based on the following articles.

### Article 1

*Plasma regions, charged dust and field-aligned currents near Enceladus*

**I.A.D. Engelhardt**, J.-E. Wahlund, D.J. Andrews, A.I. Eriksson, S. Ye, W.S. Kurth, D.A. Gurnett, M.W. Morooka, W.M. Farrell, M.K. Dougherty  
Planetary and Space Science 117 (2015), 453-469

### Article 2

*Cold and warm electrons at comet 67P/Churyumov-Gerasimenko*

A.I. Eriksson, **I.A.D. Engelhardt**, N.J.T. Edberg, F.L. Johansson, E. Odelstad, E. Vigren, J.-E. Wahlund, P. Henri, J.-P. Lebreton, W. Miloch, J.J.P. Paulsson, C. Simon Wedlund, L. Yang  
Astronomy & Astrophysics 605, A15 (2017)

### Article 3

*Plasma Density Structures at 67P/Churyumov-Gerasimenko*

**I.A.D. Engelhardt**, A.I. Eriksson, G. Stenberg Wieser, C. Goetz, M. Rubin, P. Henri, H. Nilsson, E. Odelstad, R. Hajra, and X. Vallières  
Monthly Notices of the Royal Astronomical Society, Volume 477, Issue 1, June 2018

### Article 4

*Cold Electrons at Comet 67P/Churyumov-Gerasimenko*

**I.A.D. Engelhardt**, A.I. Eriksson, E. Vigren, P. Henri, N. Gilet, X. Vallières and M. Rubin  
Submitted to Astronomy & Astrophysics

Reprints were made with the permission of the publishers.

They are available at:

Article 1: <http://doi.org/10.1016/j.pss.2015.09.010>

Article 2: <http://doi.org/10.1051/0004-6361/201630159>

Article 3: <http://doi.org/10.1093/mnras/sty765>

Papers not included in this thesis:

- *CME impact on comet 67P/Churyumov-Gerasimenko*  
N J. T. Edberg, M. Alho, M. André, D.J. Andrews, E. Behar, J.L. Burch, C.M. Carr, E. Cupido, **I.A.D. Engelhardt**, A.I. Eriksson, K.-H. Glassmeier, C. Goetz, R. Goldstein, P. Henri, F.L. Johansson, C. Koenders, K. Mandt, C. Möstl, H. Nilsson, E. Odelstad, I. Richter, C. Simon Wedlund, G. Stenberg Wieser, K. Szego, E. Vigren, M. Volwerk  
Monthly Notices of the Royal Astronomical Society, Volume 462, Issue Suppl 1, 16 November 2016, Pages S45–S56, <https://doi.org/10.1093/mnras/stw2112>
- *Effective ion speeds at 200-250 km from comet 67P/Churyumov-Gerasimenko near perihelion*  
E. Vigren, M. André, N. Edberg, **I.A.D. Engelhardt**, A.I. Eriksson, M. Galand, C. Goetz, P. Henri, K. Heritier, F.L. Johansson, E. Odelstad, M. Rubin, G. Stenberg-Wieser, C.-Y.Tzou, X. Vallières  
Monthly Notices of the Royal Astronomical Society, Volume 469, Issue Suppl 2, 21 July 2017, Pages S142–S148, <https://doi.org/10.1093/mnras/stx1472>





# Contents

|                       |          |
|-----------------------|----------|
| <b>Foreword</b> ..... | <b>v</b> |
|-----------------------|----------|

|                               |            |
|-------------------------------|------------|
| <b>List of Articles</b> ..... | <b>vii</b> |
|-------------------------------|------------|

## I

## Introduction

|          |                                                           |           |
|----------|-----------------------------------------------------------|-----------|
| <b>1</b> | <b>Introduction to the Thesis</b> .....                   | <b>3</b>  |
| <b>2</b> | <b>Plasma and Plasma Instruments</b> .....                | <b>7</b>  |
| 2.1      | Space Plasma                                              | 7         |
| 2.2      | Plasma Measurements with a Langmuir Probe                 | 8         |
| 2.2.1    | Probe Currents .....                                      | 9         |
| 2.2.2    | Electric Field Measurements with the Langmuir probe ..... | 13        |
| <b>3</b> | <b>Dust Measurements</b> .....                            | <b>15</b> |
| 3.1      | Introduction                                              | 15        |
| 3.2      | Dust Measurement Methods                                  | 17        |
| 3.2.1    | Electron vs. Ion Current .....                            | 17        |
| 3.2.2    | Direct Dust Hits .....                                    | 18        |

|            |                                                           |           |
|------------|-----------------------------------------------------------|-----------|
| <b>II</b>  | <b>Enceladus</b>                                          |           |
| <b>4</b>   | <b>Cassini - Mission and Instruments</b>                  | <b>23</b> |
| <b>4.1</b> | <b>Mission</b>                                            | <b>23</b> |
| <b>4.2</b> | <b>Instruments</b>                                        | <b>24</b> |
| 4.2.1      | Radio and Plasma Wave Science                             | 24        |
| 4.2.2      | Magnetometer                                              | 27        |
| <b>5</b>   | <b>Enceladus Environment</b>                              | <b>29</b> |
| <b>6</b>   | <b>Article 1</b>                                          | <b>33</b> |
| <b>III</b> | <b>67P/Churyumov-Gerasimenko</b>                          |           |
| <b>7</b>   | <b>Rosetta - Mission and Instruments</b>                  | <b>41</b> |
| <b>7.1</b> | <b>Mission</b>                                            | <b>41</b> |
| <b>7.2</b> | <b>Instruments</b>                                        | <b>42</b> |
| 7.2.1      | Rosetta Plasma Consortium                                 | 42        |
| 7.2.2      | Rosetta Orbiter Spectrometer for Ion and Neutral Analysis | 47        |
| <b>8</b>   | <b>Comet Environment</b>                                  | <b>49</b> |
| <b>8.1</b> | <b>Comet Plasma Physics (Pre-Rosetta)</b>                 | <b>49</b> |
| 8.1.1      | General Background                                        | 49        |
| 8.1.2      | Comet Atmosphere and Coma                                 | 51        |
| 8.1.3      | Comet Ionosphere                                          | 52        |
| 8.1.4      | Solar Wind Interaction                                    | 55        |
| <b>8.2</b> | <b>Updates from Rosetta</b>                               | <b>58</b> |
| <b>9</b>   | <b>Article 2</b>                                          | <b>63</b> |
| <b>10</b>  | <b>Article 3</b>                                          | <b>67</b> |
| <b>11</b>  | <b>Article 4</b>                                          | <b>71</b> |
| <b>IV</b>  | <b>Coda</b>                                               |           |
| <b>12</b>  | <b>Enceladus and 67P</b>                                  | <b>77</b> |

V

Backmatter

Swedish Summary ..... 81

Acknowledgements ..... 83

Acronyms ..... 85

Bibliography ..... 87

VI

Articles

Article 1 .....

Article 2 .....

Article 3 .....

Article 4 .....





# Introduction

|          |                                            |           |
|----------|--------------------------------------------|-----------|
| <b>1</b> | <b>Introduction to the Thesis .....</b>    | <b>3</b>  |
| <b>2</b> | <b>Plasma and Plasma Instruments .....</b> | <b>7</b>  |
| 2.1      | Space Plasma                               |           |
| 2.2      | Plasma Measurements with a Langmuir Probe  |           |
| <b>3</b> | <b>Dust Measurements .....</b>             | <b>15</b> |
| 3.1      | Introduction                               |           |
| 3.2      | Dust Measurement Methods                   |           |



# 1. Introduction to the Thesis

*Space is big. You just won't believe how vastly, hugely, mind-bogglingly big it is. I mean, you may think it's a long way down the road to the chemist's, but that's just peanuts to space.*

---

Douglas Adams, The Hitchhiker's Guide to the Galaxy

The topic of this thesis is the plasma and dust environment around Saturn's moon Enceladus as well as comet 67P/Churyumov-Gerasimenko (hereafter called 67P). These are two representatives for respectively icy moons and comets. These two seemingly different objects do have common features that can allow us to acquire a more general view on planet/comet formation as well as plasma processes around icy bodies at play. Both Enceladus and comet 67P/Churyumov-Gerasimenko (67P) are outgassing, albeit due to different reasons. We use the instruments that are situated on Cassini and Rosetta, visiting Saturn with its moons and 67P, respectively. Here follows a very short general introduction to Enceladus and 67P.

## **Enceladus**

Enceladus is the 6th largest ( $R = 252$  km) moon orbiting Saturn in the densest part of the E-ring at  $\sim 4R_S$ , where  $1R_S \approx 58\,000$  km is Saturn's mean radius (Thomas et al., 2007). It was first discovered in 1789 by William Herschel. Enceladus became famous after the first Cassini flyby data provided evidence that Enceladus is a geologically active icy moon. It spews out gas and dust from its southern hemisphere in the form of a plume, see fig. 1.1 (e.g. Dougherty et al., 2006; Spitale & Porco, 2007). The plume contains smaller scale structures which can be observed in

the form of jets of gas and dust that leave Enceladus through surface cracks. These surface cracks, called Tiger stripes, are young and are much warmer than the surrounding surface, covered by ice (Burger et al., 2007). Under the ice is an ocean. The outgassing of Enceladus is believed to be the major source of the gas and dust in the E-ring of Saturn, where the icy moon resides, (Kurth et al., 2006; Spahn et al., 2006a; Kempf et al., 2006). The plume has been a target for study since it was first discovered by Cassini. In total there have been 23 Cassini flybys of Enceladus.

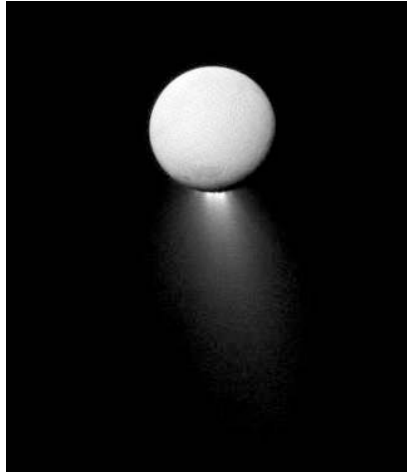


Figure 1.1: The Saturn-facing hemisphere of Enceladus (north on Enceladus is up) with the Cassini spacecraft narrow-angle camera on April 2, 2013. Image Credit: NASA/JPL-Caltech/Space Science Institute (PIA17129).

### **67P/Churyumov-Gerasimenko**

The comet was discovered in 1969 by Klim Ivanovich Churyumov and Svetlana Ivanovna Gerasimenko. Before the Rosetta mission, not much was known of this object. It used to be a member of the Kuiper belt and has currently an orbital period of 6.45 years with a rotation period of  $\sim 12.4$  hours (Mottola et al., 2014). The comet nucleus is made of two lobes and its shape reminds one of a rubber duck. Its size is about  $4.5 \times 2.5 \times 2$  km along its principal axes (Preusker, F. et al., 2017). A picture of the nucleus is shown in fig. 1.2. Rosetta followed the comet from August 5, 2014 up to September 30, 2016. During this time a heliocentric distance was covered from 3.2 AU, past a perihelion distance of 1.25 AU, August 13, 2015 and then out to 3.6 AU again (Taylor et al., 2017).



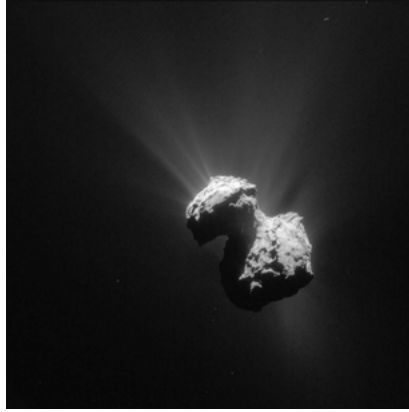


Figure 1.2: 67P/Churyumov-Gerasimenko pictured on July 7, 2015 with the NAVCAM onboard Rosetta taken from a distance of 154 km from the comet centre. Image Credit: ESA/Rosetta/NAVCAM - CC BY-SA IGO 3.0. (Id 343949).

As all objects in the solar system, these two objects as well as the spacecraft are immersed in a plasma environment. The environment of the comet is interacting with the solar wind while the plasma environment for Enceladus is Saturn's magnetosphere, which in turn is driven by the solar wind, and the magnetic field of Saturn. However, the gas and dust from both objects strongly influence their local environments, setting the overall topic for this thesis.

This part of the thesis concludes with a short introduction to plasma and plasma instruments, chapter 2. Part II and III of this thesis include introductions to the two missions and the used instruments, an introduction of the known environments and interactions as well as a summary of paper(s). Part II consists of chapters related to Enceladus. Part III is devoted to 67P/Churyumov-Gerasimenko. In Part IV we briefly summarize the similarities and differences of the two chosen objects, relevant to the thesis. Part V concludes with acronyms and references and in Part VI the collection of articles and manuscripts is attached.





## 2. Plasma and Plasma Instruments

### 2.1 Space Plasma

#### Plasma

A plasma is considered as the fourth state of matter. It is a quasi-neutral ionized gas consisting of charged as well as neutral particles. It exhibits collective behavior meaning that it is governed by large-scale collective motions.

Both spacecraft used in the thesis have several instruments on board that measure various plasma parameters. These parameters can for example include the magnetic and electric field, electron and ion density, temperatures, and plasma wave spectra. See sections 4.2 and 7.2 for a short overview of Cassini and Rosetta instruments, respectively.

Plasma is all around our Earth, in our solar system and beyond. Earth has an intrinsic magnetic field which interacts with the interplanetary magnetic field and the solar wind, to form the magnetosphere. Not only Earth has a magnetosphere but also other magnetized planets. Also unmagnetized planets like Venus and Mars get a kind of magnetosphere, by the process of mass loading and draping which will be discussed below and in section 8.1.4.

Inside Saturn's magnetosphere lies the moon Enceladus. Enceladus does not have an internal magnetic field but is nevertheless subject to space plasma interactions. This is due to the atmosphere/ionosphere around it. The material comes from the southern hemisphere and interacts with Saturn's rotating magnetosphere. As the magnetosphere passes by it "feels" the presence of the moon and the ionized material. These particles are interacting with the

magnetospheric flow as these get accelerated, slowing down the flow locally until particles have the same velocity as the magnetospheric flow. This effect is called mass loading and does go hand in hand with the effect of so called magnetic field draping: As the magnetospheric flow arrives at a conducting obstacle, the plasma and so the magnetic field is diverted around this object. (See discussion in section 8.1.4).

For the comet, similar processes take place. Just like the moon, the comet does not have an intrinsic magnetic field, such as the moon, but interacts directly with the solar wind. When the comet is active, it has an ionosphere that is interacting with the solar wind. Due to the heating of the comet, it starts outgassing material that gets ionized and then interacts with the solar wind. This leads to mass loading and very strong magnetic draping forming a magnetic tail, even though the comet nucleus has no magnetic field of its own. These objects are not only surrounded by pure plasma but they also contain dust of various sorts, which leads to plasma-dust interactions.

## 2.2 Plasma Measurements with a Langmuir Probe

This section concentrates on the plasma measurements done by a Langmuir probe since this is the main instrument used throughout the thesis. The Langmuir probe instruments are called LP on Cassini and LAP on Rosetta. Short summaries of the two instruments can be found in the articles' method/instrumentation sections.

The Langmuir probes (and the spacecraft) are immersed in a plasma. By setting the probe to a specific potential it measures the current that results from charged particles being attracted to, or repelled from the probe. These currents are described by the orbit motion limited (OML) theory considering the distribution of particles moving in a vacuum field from a probe on trajectories determined by conservation of energy and angular momentum alone (Engwall, 2006). OML currents are the largest possible currents collected by a perfectly absorbing probe in a collisionless, stationary plasma (Grard, 1973). For OML theory to hold, the probe radius must be much smaller than the Debye length,  $\lambda_D$ , otherwise the space charge in the sheath shields the probe potential from the plasma. This results in lower currents than in the OML case. For the plasmas studied in this thesis, OML is applicable. Furthermore, the probes are always smaller than the particle gyroradius, allowing us to neglect the magnetic field.

There are three main operational modes used in space science for a Langmuir probe. For one, a constant bias voltage is applied to the probe measuring the current with a specific amount of samples per seconds (on Cassini 20 samples per second, on Rosetta up to 57.8 samples per second). This mode is useful for

following dust or small-scale variations in the plasma. The second mode is a voltage sweep (on Cassini usually 512 steps from -32 V to +32 V, on Rosetta 240 steps or less over a similar voltage range). Sweeps are used to derive further plasma characteristics such as electron temperature and spacecraft potential. The third mode is known as an electric field mode where a current is set to two probes and the resulting voltage is measured. The E-field can then be derived from the voltage difference of the two probes. This is only applicable to Rosetta since Cassini does have only one probe.

The basic currents to a probe are the electron current, the ion current and the photoelectron current (Holmberg, 2013). As the probe is not fully isolated in space but mounted on a spacecraft, the probe current is also influenced to some degree by perturbations arising from the spacecraft plasma interaction. To minimize this, the probes are mounted on booms (1.5 m on Cassini and 2.2 and 1.6 m on Rosetta).

A free floating probe, with no set voltage, in space will charge to some equilibrium potential by the currents flowing to it from the particle populations (e.g. ions and electrons) in the plasma. When this equilibrium potential is reached, the total current to the probe must be zero, so the currents from the various sources balance each other, if we consider the whole spacecraft as one free floating probe. This is known as the spacecraft potential. In principle, the spacecraft itself is a large Langmuir probe as it collects charges.

## 2.2.1 Probe Currents

A probe in a dense ionospheric plasma is coupled to the local plasma by several kinds of currents. In the following sections we introduce the most important of these. The OML theory for these currents was originally developed by Mott-Smith & Langmuir (1926), with various extensions by later authors. We will here use the summary for spherical probes by Engwall (2006) which is useful for our kind of instruments. For references to original articles please see Engwall (2006).

### 2.2.1.1 Thermal Current

When the potential of the probe is zero with respect to the surrounding plasma, each particle species in the plasma will carry a current to it. This current is due to the random thermal motion of the particles, and henceforth called thermal current. The thermal current for a given particle species with Maxwellian distribution is given by

$$I = nqA_{LP}\sqrt{\frac{k_b T}{2\pi m}} \equiv I_{th}. \quad (2.1)$$

Here  $A_{LP} = 4\pi r_{LP}^2$  is the Langmuir probe surface area and  $r_{LP}$  the radius. Furthermore we have the particle's charge  $q$ , the number density  $n$ , the Boltzmann constant  $k_b$ , the temperature  $T$ , in Kelvin, and the particle mass  $m$ , depending on the species. There are thermal currents due to ions as well as electrons but a probe with no set potential will usually be charged negative since electrons are generally much faster due to their lower mass and therefore higher mobility.

### 2.2.1.2 Currents to a Charged Probe

By charging the probe to a specific probe potential  $U_p$  with respect to the plasma, it will be shielded by charges of opposite sign and create a sheath/cloud around it. As long as the size of the probe is much smaller than the Debye length,  $r_p \ll \lambda_D$ , the shielding will be weak and the charge in this sheath cannot significantly change the potential.

The particle energy distribution is assumed to be a Boltzmann distribution and the current to a probe at attractive potentials,  $qU_p < 0$ , is given by

$$I_\alpha = I_{\alpha,th}(1 - \chi_\alpha) \quad (2.2)$$

and at repulsive potentials,  $qU_p > 0$ , is given by

$$I_\alpha = I_{\alpha,th}e^{-\chi_\alpha} \quad (2.3)$$

where

$$\chi_\alpha = \frac{q_\alpha U_p}{k_b T_\alpha} \quad (2.4)$$

with  $\alpha = i, e$  depending on the species in question. Here we write  $U_p = U_{SC} + U_b$ , where  $U_{SC}$  is the spacecraft potential and  $U_b$  the potential of the probe with respect to the spacecraft. This is the potential that can be controlled by a Langmuir probe instrument.

The repulsive current, eq. (2.3), describes that there exist some particles with high enough energy or velocity that can overcome the potential barrier and still contribute to the total current.

### 2.2.1.3 Currents in a Flowing Plasma

Langmuir probes mounted on spacecraft are moving through space and the plasma at a certain velocity. Thus there is a relative velocity between the probe and the plasma. Even if one would have a stationary spacecraft, a relative velocity can still be accomplished by a moving plasma. This is the case for example at Saturn, where most of the inner magnetosphere is (more or less perfectly) co-rotating with the planet.

If the drift speed is comparable to the thermal speed a term for the drift speed,  $v$ , needs to be added in the thermal current (see red term) (Engwall, 2006, reproduced) which can be approximately written as

$$I_{\alpha,th} = n_{\alpha} q_{\alpha} A_{LP} \sqrt{\frac{k_b T_{\alpha}}{2\pi m_{\alpha}} + \frac{v_{\alpha}^2}{16}} \quad (2.5)$$

as well as in the expression for  $\chi$ :

$$\chi_{\alpha} = \frac{q_{\alpha} U_p}{k_b T_{\alpha} + \frac{m_{\alpha} v_{\alpha}^2}{2}} \quad (2.6)$$

For our cases, we only need to consider this for ions, because the electron thermal speed is much larger than the plasma drift speed with respect to the spacecraft both at Enceladus and around comet 67P.

### 2.2.1.4 Photoelectron Current

In a sufficiently tenuous plasma, such as in the Earth's magnetotail, the photoelectron current is dominating. Photoelectrons are electrons that are knocked out from a (spacecraft-) surface due to photons with energy above the electron binding energy, in practice meaning EUV or shorter wavelengths. Photoelectron current can show up in the current measurements in two ways. One is the photoemission current from the probe itself and the other is an electron current due to photoelectrons being emitted from other parts of the spacecraft and then collected by the probe.

For a probe at negative potential, all emitted photoelectrons escape and will not come back to the probe. The photoelectron current reaches a saturation level. However if the probe is at a positive potential, electrons are freed by the photons, but some of them will be attracted back to the probe, depending on their energy. For an exponential (Boltzmann-like) energy distribution of the emitted photoelectrons, this causes an exponential decrease in the current.

The magnitude of the photoelectron current depends on different parameters such as the distance to the Sun, the size of the sunlit area, the surface properties of that and the solar activity. The photo yield (produced photoelectrons per incoming photon) is mainly a function of the material (Pedersen, 1995). The probes on Cassini and Rosetta for example are made of titanium with a titanium nitride coating.

### 2.2.1.5 Current Summary

Figure 2.1 shows a summary of possible particles hitting the probe. Here we have ambient electrons, ions, photoelectrons from the probe (leaving) and photoelectrons coming from the spacecraft (arriving). Figure 2.2 shows an example of the resulting current signature (red line) of a sweep. It is comprised of the electron- (blue dashed), ion- (yellow dashed) and photoelectron- (green dot dashed) current contributions.

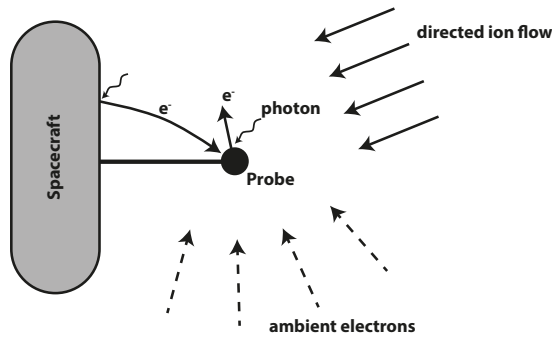


Figure 2.1: Four types of current that can contribute to the probe characteristics: (1) ambient electrons, (2) directed ion flow (due to the surrounding plasma and spacecraft motion), (3) photoelectrons from the probe, and (4) photoelectrons from the spacecraft. Adapted from Olson et al. (2010, Fig. 7.), with permission from Elsevier.

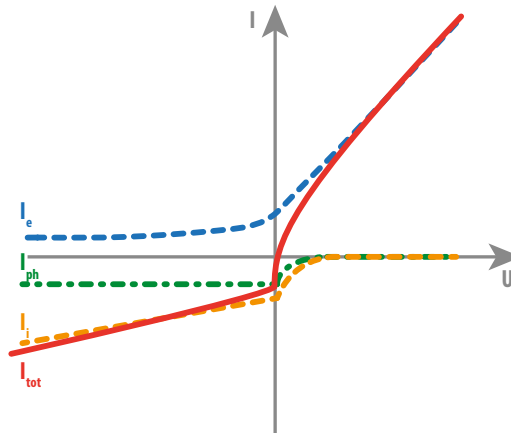


Figure 2.2: This figure shows an example of the current contributions in a sweep from the electron (blue dashed), ion (yellow dashed) and photoelectron (green dot-dash) current as well as the resulting total current (red solid line).



### 2.2.2 Electric Field Measurements with the Langmuir probe

Because the plasma consists of charged particles, magnetic and electric fields are central to the dynamics. To measure the electric field two probes are fed with the same bias current. The electric field can then be found by measuring the voltage difference between the two spherical sensors divided by their effective separation (Pedersen et al., 1998). The physical separation or distance between the two probes however needs to be long enough for the signals of the electric field in the plasma to overcome perturbations from the spacecraft-like noise from its electrons, charging of its surfaces, inhomogeneities in its photoelectron cloud and wake effects of the plasma flying by. With the double probe technique one can measure electric fields over a large dynamic range with high time resolution and simplicity. A by-product of the electric field measurements is an estimate of the spacecraft potential  $U_S$  at high time resolution, by taking the negative average of the two probe voltages instead of their difference. This is how data from this mode are used in article 3 (chapter 10).





## 3. Dust Measurements

### 3.1 Introduction

Saturn's rings are a nice example of the co-existence of dust and plasma in space. One can distinguish two cases (Merlino, 2006). The first is when only a few isolated dust particles are in the plasma with little to no feedback from the dust on the plasma dynamics. This is known as the "dust in plasma" case. In the second case, actually called the "dusty plasma", are a large number of dust particles that do interact with, and alter the properties and collective behavior of the plasma.

In the literature, a dusty plasma is also called a complex plasma (Ishihara, 2007). The constituents of such a plasma are neutral gas molecules, electrons, ions and massive<sup>1</sup> charged dust grains (Shukla, 2001; Ishihara, 2007).

The dust grains can range in size from tens of nanometers to hundreds of microns, they can come in any shape and may be composed of dielectrics or conducting materials, see as an example dust observed by Rosetta Cometary Secondary Ion Mass Analyzer (COSIMA) instrument, fig. 3.1. They don't have to be solid but can also be fluffy ice crystals or even liquid droplets, although the latter case is unlikely in space as liquids are usually not stable at the low pressures around.

Charging of a dust particle can happen in several ways, for example bombardment of dust grains by plasma particles<sup>2</sup>, photoemission by UV radiation, ion

---

<sup>1</sup>Dust particles are massive compared to ion masses.

<sup>2</sup>Electrons and Ions

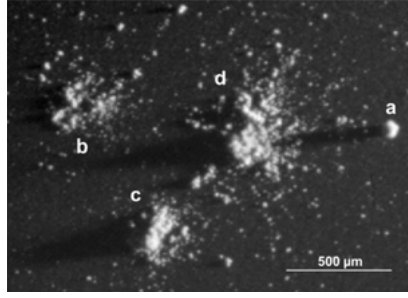


Figure 3.1: Diversity of particles seen on a small area on one single target. This image section measures 2.5 mm across, with light coming from the right. Examples of a compact particle (a), a shattered cluster (b), a glued cluster (c) and a large rubble pile (d) are seen in this small area. Image credit: ESA/Rosetta/MPS for COSIMA Team MPS/CSNSM/UNIBW/TUORLA/IWF/IAS/ESA/BUW/MPE/LPC2E/LCM/FMI/ UTU/LISA/UOFC/vH&S/ Langevin et al. (2016, Fig. 10), with permission from Elsevier.

sputtering and secondary electron production. A dust particle can become negatively or positively charged, depending on which process is dominating. Positive and negative grains may coexist because of different size, material, structure and history. An isolated dust grain that is shielded from any radiation acquires a negative average charge, if the ion and electron number densities ( $n_e = n_i$ ) as well as the ion and electron temperatures ( $T = T_e = T_i$ ) are equal (Horányi et al., 2004). Since electrons are much faster compared to ions, the potential on the surface of the dust particle becomes negative with respect to the potential of the plasma far from the dust particle. In equilibrium the charge on the dust grain  $q_d$  (Horányi et al., 2004) will be given by

$$q_d = -4\pi\epsilon_0 r_d \alpha \frac{k_b T}{e} \quad (3.1)$$

where  $\epsilon_0$  is the vacuum permittivity,  $r_d$  is the radius of the dust grain assumed to be spherical,  $k_b$  is the Boltzmann constant, and  $T$  the temperature given in [K]. The proportionality factor  $\alpha$  is of the order of 1 and a function of the ion mass  $m_i$ .

Dust has a strong influence on collective effects, if the dust carries a significant fraction of charge; either negative or positive. The Havnes parameter<sup>3</sup> has been introduced as an indicator if the charge carries a significant amount of negative charge in a plasma. Photoelectric emission from dust is ignored and the Havnes

<sup>3</sup>There exist several different definitions of this parameter.

parameter is given by (Ishihara, 2007)

$$P = \frac{|Z_d|n_d}{n_e} \quad (3.2)$$

where  $Z_d$  is the dust charge number. If  $P \ll 1$ , the dust will carry only a small fraction of the negative charge, and the single particle approximation, eq. (3.1), can be used to find the average charging of a grain (Horányi et al., 2004). Collective effects will become dominant if the Havnes parameter becomes large,  $P \geq 1$  (Ishihara, 2007).

## 3.2 Dust Measurement Methods

There are different ways of measuring dust. Every method has its limitations. We present here only methods with the means of a Langmuir probe and electric antenna, or any electric receiver/antenna. Other dust experiments purely devoted to dust do exist as well. On both Cassini and Rosetta they are mainly sensitive to larger grains which are fewer in number and not as strongly interacting with the plasma (Wahlund et al., 2009; Morooka et al., 2011; Shafiq et al., 2011; Rotundi et al., 2015).

### 3.2.1 Electron vs. Ion Current

A relatively simple way to infer (smaller) dust grains in the plasma environment is by comparing the electron and ion densities,  $n_e$  and  $n_i$ , respectively. Quasineutrality in a regular plasma is given by

$$q_i n_i = e n_e. \quad (3.3)$$

In a dusty plasma however, the quasineutrality equation is appended with a contribution of the dust. Assuming dust to be negatively charged due to the higher probability of collecting electrons than ions from the neighborhood, as well as assuming the electron and ion charge to be of equal magnitude,  $q_i = e$ , the quasineutrality relation (Morooka et al., 2011; Shukla, 2001) is then given by

$$n_i = n_e + |Z_d|n_d. \quad (3.4)$$

Dust can be indirectly inferred by means of comparison of electron and ion density. When the ion density is constant over some time while the electron density decreases, it means that the dust density component in the quasineutrality equation must increase, eq. (3.4). This is due to the attachment of electrons to

dust grains (Morooka et al., 2011). Figure 3.2 shows an example of this simple method. The upper panel shows the electron (blue) and ion (red) density of flyby E2 from Cassini, (more in chapter 6). Subtracting these gives the charged dust density as in eq. (3.4). It is clear, that around 19:55, where ion and electron density differ the most, the charged dust density is largest.

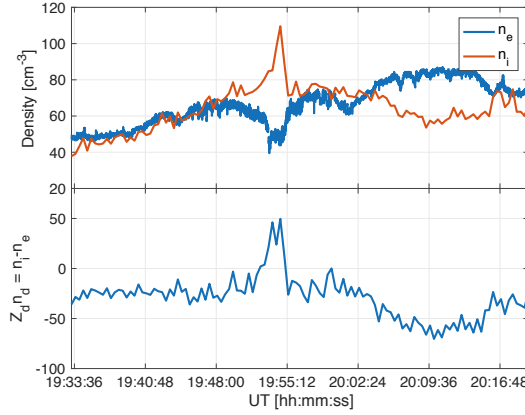


Figure 3.2: Example of a comparison between electron and ion density, and the result of charged dust density for Cassini flyby of Enceladus, July 14 2005. The upper panel shows the electron (black) and ion (blue) density. The lower panel shows the dust density as a result of subtracting electron from ion density.

This method should in principle also be possible to use for Rosetta at comet 67P. However, as Rosetta moves much slower than Cassini (typically less than a m/s), it has not yet been possible to obtain the ion density sufficiently accurate to get a reliable difference between  $n_i$  and  $n_e$ . This is because the ion velocity needs to be known (eq. (2.5)). Further detailed studies of Rosetta data may make this possible.

### 3.2.2 Direct Dust Hits

Plasma wave instruments are sensitive to micron-sized dust impacts on a spacecraft (Kurth et al., 2006). Dust impacts result in a voltage pulse in the signal from electric field antenna, that can be counted to give an accurate measure of the dust impact rate. The size of particles can be estimated through the amplitude of the voltage pulse.

The mechanism for the voltage pulse was given by Kurth et al. (2006) as follows. With high enough relative velocity between the particles and the spacecraft, the particle and part of the targets material is vaporized and partially ionized. This

ionized cloud expands and results in an ambipolar electric field that results in a voltage pulse (see fig. 3.3a). The magnitude of the voltage pulse is proportional to the mass of the impacting particle as well as a function of the velocity of the impact. Another likely dependence exist with the target material. Figure 3.3b shows an example of those dust hits.

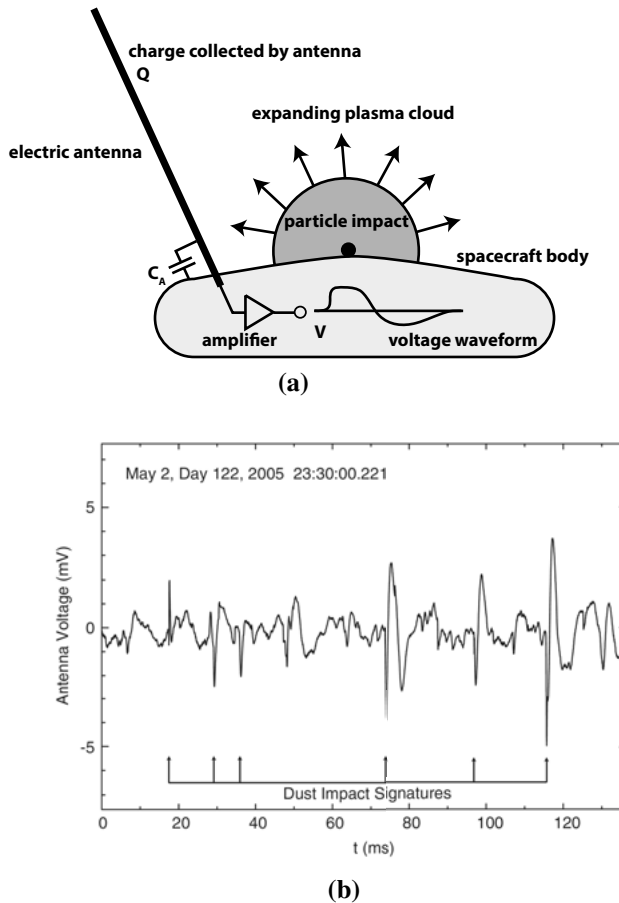


Figure 3.3: (a) Schematics adapted from Gurnett et al. (1983, fig. 8) showing a plasma cloud produced by impact ionization and resulting in a voltage pulse. (b) Typical signature of E-ring dust observed by the Radio and Plasma Wave Science (RPWS) on Cassini. Reused from Kurth et al. (2006, fig. 1). Both figures are reproduced with permission from Elsevier.

Usually the data is Fourier transformed on board and these pulses then appear as a broad band emission in the spectrum. This can then be used to infer dust impacts (Wang et al., 2006). Figure 3.4 shows a typical signature of Cassini flying through a dusty region near Enceladus.

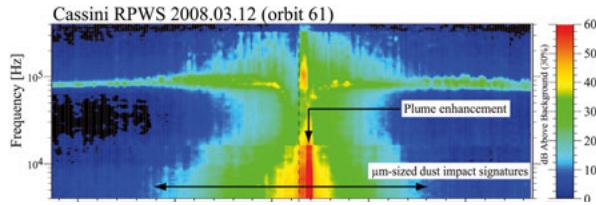
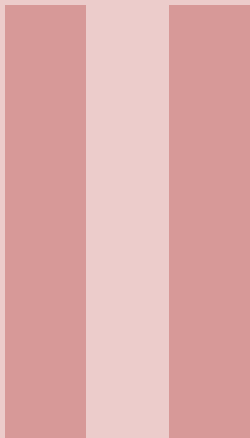


Figure 3.4: Schematics taken from Morooka et al. (2011, fig. 1), with permission from Elsevier, showing a typical spectrum of a dusty region near Enceladus, recorded with Cassini. This figure is cropped and the x-axis is flight time of totally 24 minutes.

This method will not work on Rosetta, as the typical dust speed there is about 1 m/s (Rotundi et al., 2015). This means dust hits on the spacecraft are better described as soft landings rather than impacts, and should not lead to ionization. Current pulses seen in Rosetta Langmuir probe (LAP) data were first thought to be due to dust, but as discussed in article 2 and 3 (chapters 9 and 10) this cannot really be the case. They must instead be due to local plasma variations.





# Enceladus

|          |                                                    |           |
|----------|----------------------------------------------------|-----------|
| <b>4</b> | <b>Cassini - Mission and Instruments . . . . .</b> | <b>23</b> |
| 4.1      | Mission                                            |           |
| 4.2      | Instruments                                        |           |
| <b>5</b> | <b>Enceladus Environment . . . . .</b>             | <b>29</b> |
| <b>6</b> | <b>Article 1 . . . . .</b>                         | <b>33</b> |



A detailed illustration of the Cassini spacecraft in orbit around Saturn. The spacecraft is shown from a side-on perspective, with its complex structure of antennas, solar panels, and instruments clearly visible. Saturn's large, white, cloud-covered disk dominates the right side of the frame, while the dark, star-filled background of space fills the rest. A red-bordered white banner is overlaid on the bottom left of the image, containing the section title.

## 4. Cassini - Mission and Instruments

### 4.1 Mission

The objective of the Cassini-Huygens mission is to study Saturn and its icy moons such as Titan. It consists of the Cassini spacecraft and the Huygens probe and is a joint project between NASA, ESA and ASI. Launched for its mission to Saturn on the 15th of October 1997 from Cape Canaveral in Florida, it arrived at Saturn in 2004 (Pailharey & Vignaux, 2004; NASA - JPL, 2012). The Huygens probe was separated 25th of December 2004 from Cassini and landed on Titan 14th of January 2005. Cassini was left to orbit Saturn and its moons.

It started with the four year prime mission which lasted from July 2004 to July 2008. After successful operation and good state of health NASA granted two mission extensions. The first one was called the Equinox mission, from July 2008 to October 2010 and the second extension, the Solstice mission, was planned until September 2017. The last part of the Solstice mission is called 'The Grand Finale'. With that Cassini orbited Saturn closer and finally was sent to burn in its atmosphere 15th of September 2017. Table 4.1 shows the timeline of Cassini and Huygens. The instrumentation is summarized in the following sections.

| Date [dd-mm-yyyy] | Description                                             |
|-------------------|---------------------------------------------------------|
| 15-10-1997        | Launch                                                  |
| 07-2004           | Arrival at Saturn and mission start                     |
| 25-12-2004        | Lander separation                                       |
| 14-01-2005        | Huygens lands on Titan                                  |
| 07-2008           | End of main mission and<br>start of Equinox mission     |
| 10-2010           | End of Equinox mission and<br>start of Solstice mission |
| 15-09-2017        | End of Solstice mission                                 |

Table 4.1: Overview of Cassini-Huygens timeline

## 4.2 Instruments

The Cassini spacecraft carries 12 different instrument groups and the Huygens probe is equipped with another 6 instrument groups, see tables 4.2 and 4.3, respectively.

The main instrument groups used for this investigation/study are the RPWS (P.I. institute: University of Iowa) and Magnetometer (MAG) (P.I. institute: Imperial College London). The instruments of these groups are explained in more detail in the following sections.

### 4.2.1 RPWS - Radio and Plasma Wave Science

The RPWS includes electric field sensors, a magnetic search coil assembly, a spectrum analyzer and a Langmuir probe (NASA - JPL, 2012; Gurnett et al., 2004). The location of the instruments of the RPWS is shown in fig. 4.1.

#### 4.2.1.1 Langmuir probe

The Langmuir probe (LP), provided by the Swedish Institute of Space Physics (IRF), is a titanium sphere with a titanium nitride coating, of 5 cm in diameter and it measures resulting currents between the plasma and the probe while it is set to a given potential. From that data one can infer the electron temperature, electron density and estimate the potential of the spacecraft with respect to the plasma (Wahlund et al., 2009). In the deployed configuration, the LP itself is about 1.5 m away from the closest spacecraft surface (Gurnett et al., 2004).

| Acronym | Full Name                                 |
|---------|-------------------------------------------|
| CAPS    | Cassini Plasma Spectrometer               |
| CDA     | Cosmic Dust Analyzer                      |
| CIRS    | Composite Infrared Spectrometer           |
| INMS    | Ion and Neutral Mass Spectrometer         |
| ISS     | Imaging Science Subsystem                 |
| MAG     | Magnetometer                              |
| MIMI    | Magnetospheric Imaging Instrument         |
| RADAR   | Cassini Radar                             |
| RPWS    | Radio and Plasma Wave Science             |
| RSS     | Radio Science System                      |
| UVIS    | Ultraviolet Imaging Spectrograph          |
| VIMS    | Visible and Infrared Mapping Spectrometer |

Table 4.2: List of the 12 instrument groups on board Cassini.

| Acronym | Full Name                                |
|---------|------------------------------------------|
| ACP     | Aerosol Collector Pyrolyzer              |
| DISR    | Descent Imager/Spectral Radiometer       |
| DWE     | Doppler Wind Experiment                  |
| GCMS    | Gas Chromatograph Mass Spectrometer      |
| HASI    | Huygens Atmospheric Structure Instrument |
| SSI     | Surface Science Package                  |

Table 4.3: List of the 6 instrument groups on board the Huygens probe.

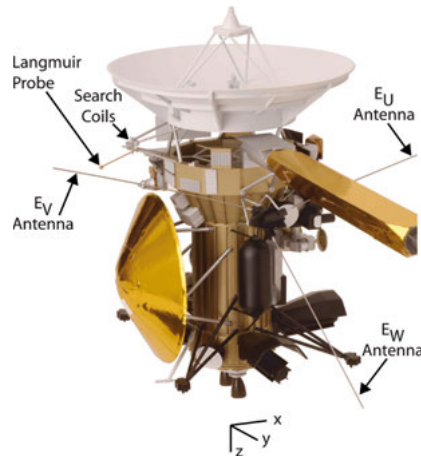


Figure 4.1: Model of the Cassini spacecraft showing the locations of the instruments of the RPWS. Reused from Gurnett et al. (2004, Figure 14), with permission from Elsevier.

The LP has two main measurement modes on the Cassini mission. The first one is a 512 point voltage sweep,  $\pm 32$  V. This mode usually operates every 10 minutes or 24 seconds for targeted flybys. (Wahlund et al., 2009). For the second mode, the bias is set to a constant voltage, usually chosen to be +11.5 V and the resulting current is measured with a sampling frequency of 20 Hz. Figure 4.2 shows a photograph of said LP with its boom assembly in stowed configuration.

More details on the underlying theory, data acquisition and analysis can be found in chapter 2.

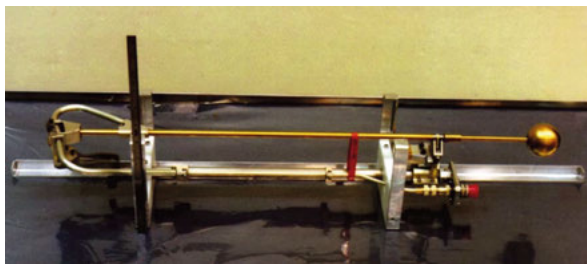


Figure 4.2: A photo of the Langmuir probe in its stowed configuration. Photo credit: IRF Uppsala.

### 4.2.1.2 Electric and Magnetic Antennas

The electric and magnetic antennas are used together with the spectrum analyzer for electron density calibration. The antennas are three 10 m long conducting cylinders with a diameter of 2.86 cm. The variation of the magnetic field is measured by a tri-axial search coil magnetic antenna. The search-coil magnetometer uses the principle of Faraday's law that a changing magnetic field induces a voltage, so it cannot measure quasi-static fields but has high sensitivity for waves. For more detailed specifications see Gurnett et al. (2004).

### 4.2.1.3 Spectrum Analyzer

The spectrum analyzer is used for dust and upper hybrid frequency detection. It consist of a high frequency receiver providing measurements from two selected antennas (3.5 kHz to 16 MHz) and a medium frequency receiver providing intensity measurements from a single selected antenna (24 Hz to 12 kHz) (Wang, 2006).

## 4.2.2 MAG - Magnetometer

The MAG instrument consists of two direct sensing magnetometers and associated electronics. It measures the magnitude and direction of the magnetic field with a fluxgate magnetometer and or a vector/scalar helium magnetometer. The data used here comes from the fluxgate magnetometer. For more information see Kellock et al. (1996).

The fluxgate magnetometer works as follows: A ferromagnetic core is driven to saturation by an AC through a driving winding. If there is an external magnetic field, the core gets biased and an asymmetric flux, proportional to the magnetic field, can be detected by a second winding, the sense winding. This asymmetry leads to harmonics of the AC frequency in the Fourier spectrum of the signal from the sense winding. These can be identified and used for deriving the magnetic field.





## 5. Enceladus Environment

Artist's concept

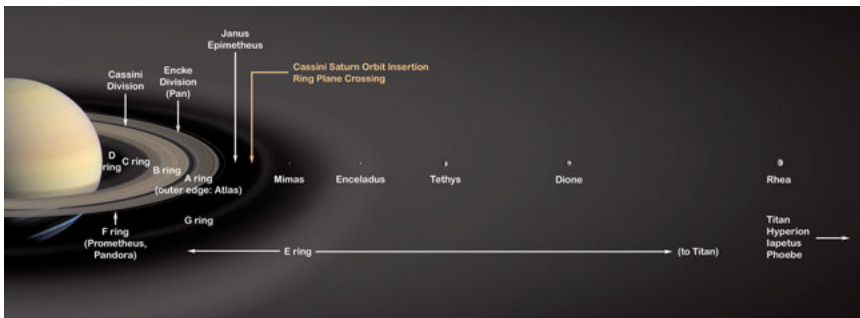


Figure 5.1: Saturn's rings and major moons. Image Credit: NASA/JPL (PIA03550)

As described in chapter 1, Enceladus lies in the densest part of the E-ring, see an illustration in fig. 5.1. Enceladus quickly became a focus of the Cassini mission after its plumes were discovered and many studies have since been conducted on the plume physics based on the Cassini observations (e.g., Spitale & Porco, 2007; Cravens et al., 2009; Krupp et al., 2012). The small icy moon is geologically active showing geysers at the south polar region that spew out gas and dust (Dougherty et al., 2006; Porco et al., 2006; Spahn et al., 2006b; Waite et al., 2006). As the gas leaves the vents it gets partially ionized and drags along negatively charged nanograins (Jones et al., 2009; Morooka et al., 2011; Shafiq et al., 2011; Hill et al., 2012; Farrell et al., 2012; Dong et al., 2015). Inside the plume, the density of the plasma constituents increases by several orders of magnitude, compared to the magnetospheric plasma flow. This newly charged material gets picked up by the plasma flow which accelerates these

particles (e.g., Tokar et al., 2006, 2008; Pontius & Hill, 2006; Fleshman et al., 2010; Farrell et al., 2012). Enceladus is believed to be the primary source of the E-ring material, such as sub-micron sized dust and negatively charged water ice (e.g., Kurth et al., 2006; Spahn et al., 2006b; Kempf et al., 2006; Hillier et al., 2007). The plume material plays an important role in the dust plasma interaction (Wahlund et al., 2005, 2009). An example of an interaction between Enceladus plume and its surroundings can be seen in fig. 5.2.



Figure 5.2: This is an image taken by the Imaging Science Subsystem (ISS) of Enceladus and it's interaction with Saturn's E-ring. The dust is seen to be disturbed by Enceladus' presence. Image Credit: NASA/JPL/Space Science InstituteL (PIA08321)

The plume is electrically conductive and forms an obstacle to the ambient plasma flow, which causes large scale perturbations in the close vicinity of Enceladus (e.g., Dougherty et al., 2006; Saur et al., 2007). These perturbations include the slow down and pile up upstream of the moon due to mass loading of the corotating plasma of Saturn by ionization of plume material (Dougherty et al., 2006; Morooka et al., 2011). Saturn's ionosphere shows signs of an auroral footprint of Enceladus. This is caused by field aligned currents between the moon and the planet that are induced by the motion of the moon with its conductive ionosphere through the magnetic field of Saturn and these are then closing through Saturn's ionosphere (Kriegel et al., 2011; Simon et al., 2014; Pryor et al., 2011). At the edge of the plume, auroral hiss emissions (Gurnett et al., 2011; Leisner et al., 2013) can be observed along the Alfvén wings caused by the moving plasma flow around a stationary conductive obstacle, the Enceladus-plume-system. These wedge shaped regions are similar to those observed at Io (Neubauer, 1980).

The magnetospheric plasma interaction with Enceladus and its plume has been modeled extensively over the years. The different approaches used are numerical models using both fluid and hybrid approximations as well as analytical models (see e.g. Jia et al., 2010; Kriegel et al., 2009; Simon et al., 2011). These models have been under constant development to include negatively charged dust grains as an important component of the plasma (Omidi et al., 2010, 2012). The most important result is the strong influence of charged dust on the Enceladus plasma interaction indicating that these interactions should not be omitted from further models (e.g., Kriegel et al., 2014; Omidi et al., 2012).





## 6. Article 1

### **Plasma regions, charged dust and field-aligned currents near Enceladus**

The first article is entitled "Plasma regions, charged dust and field-aligned currents near Enceladus" and has been published in Planetary and Space Science (Engelhardt et al., 2015). Here follows a short summary. Details about the measurements and derivations can be found in the article.

We determine the large scale plasma properties of the close vicinity of Enceladus. For this, two instrument packages were used, the LP and the Wide Band Receiver (WBR) of the RPWS as well as the fluxgate magnetometer of the MAG instrument package (both summarized in section 4.2). The full measurement method is described in the article, section 2.

For this analysis 20 flybys between the years 2005 and 2012 have been used (E0 - E19). These, and three more flybys that happened after submission of the article, are listed in table 6.0. Two of the new flybys (E20 and E22) are relatively far away from Enceladus and not part of the 'close' region we investigated in this article. Flyby E21 is a (too) close flyby over the south polar region.

The main focus is on separate plasma regions identified in the close vicinity of Enceladus. The main data for the distinction between these regions was the electron density derived from the 20 Hz LP data, which was then compared to magnetic field as well as the dust density, inferred from the electric field antenna. Here we found three main regions defined as the plume region, the plume edge region and the trail region, see fig. 6.1.

Enceladus Flybys

| Flyby | Rev | Date       | DoY | Time     | Altitude [km] | $\langle v_{s/c} \rangle$ [km/s] | Plume |
|-------|-----|------------|-----|----------|---------------|----------------------------------|-------|
| E0    | 003 | 2005-02-17 | 048 | 03:30:30 | 1264.003      | 6.7                              |       |
| E1    | 004 | 2005-03-09 | 068 | 09:08:03 | 497.034       | 6.7                              |       |
| E2    | 011 | 2005-07-14 | 195 | 19:55:22 | 165.034       | 8.2                              |       |
| E3    | 061 | 2008-03-12 | 072 | 19:06:12 | 47.674        | 14.4                             | ✓     |
| E4    | 080 | 2008-08-11 | 224 | 21:06:19 | 49.421        | 17.7                             | ✓     |
| E5    | 088 | 2008-10-09 | 283 | 19:06:40 | 24.586        | 17.7                             | ✓     |
| E6    | 091 | 2008-10-31 | 305 | 17:14:51 | 169.073       | 17.7                             | ✓     |
| E7    | 120 | 2009-11-02 | 306 | 07:41:58 | 98.909        | 7.8                              | ✓     |
| E8    | 121 | 2009-11-21 | 325 | 02:09:56 | 1596.595      | 7.8                              | ✓     |
| E9    | 130 | 2010-04-28 | 118 | 00:10:17 | 100.434       | 6.5                              | ✓     |
| E10   | 131 | 2010-05-18 | 138 | 06:04:40 | 437.068       | 6.5                              |       |
| E11   | 136 | 2010-08-13 | 225 | 22:30:52 | 2555.235      | 6.9                              | ✓     |

continued

| Flyby | Rev | Date       | DoY | Time     | Altitude [km] | $\langle v_{s/c} \rangle$ [km/s] | Plume |
|-------|-----|------------|-----|----------|---------------|----------------------------------|-------|
| E12   | 141 | 2010-11-30 | 334 | 11:53:59 | 45,763        | 6.3                              |       |
| E13   | 142 | 2010-12-21 | 355 | 01:08:27 | 48,394        | 6.3                              |       |
| E14   | 154 | 2011-10-01 | 274 | 13:52:26 | 98,906        | 7.5                              | ✓     |
| E15   | 155 | 2011-10-19 | 292 | 09:22:11 | 1230,756      | 7.5                              |       |
| E16   | 156 | 2011-11-06 | 310 | 04:58:53 | 496,578       | 7.4                              |       |
| E17   | 163 | 2012-03-27 | 087 | 18:30:09 | 74,166        | 7.5                              | ✓     |
| E18   | 164 | 2012-04-14 | 105 | 14:01:38 | 74,104        | 7.5                              | ✓     |
| E19   | 165 | 2012-05-02 | 123 | 09:31:29 | 73,133        | 7.5                              | ✓     |
| E20   | 223 | 2015-10-14 | 287 | 10:42:29 | 1844,230      | 8.5                              |       |
| E21   | 224 | 2015-10-28 | 301 | 15:23:42 | 49,037        | 8.5                              | ✓     |
| E22   | 228 | 2015-12-19 | 353 | 17:49:16 | 5000,221      | 9.5                              |       |

Table 6.0: Table of Enceladus Flybys, with the flyby number, revolution, date, day of the year, time of closest approach, altitude of closest approach, spacecraft velocity at closest approach and plume crossing.

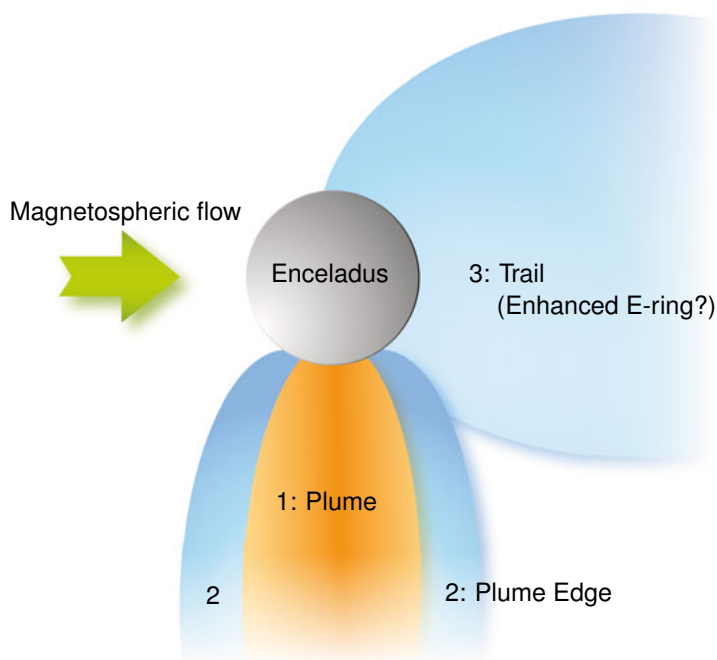


Figure 6.1: An illustration of the plasma regions studied (not to scale). Reused from Engelhardt et al. (2015, Figure 11), with permission from Elsevier.

The plume region is well known from previous studies and is characterized by an electron density increase of about 2-3 orders of magnitude (Dougherty et al., 2006; Porco et al., 2006). This region is also characterized as a mass loading and ion pick-up region with increased magnetic field due to stagnation of the plasma. This does agree with the data we have from the Langmuir probe.

The plume edge region is an electron depletion region with an electron density decrease down to  $30 \text{ cm}^{-3}$  (a drop of 50-70% compared to the background field). This has not been reported before this study.

Lastly there is the new trail region downstream of the moon where we measure an electron depletion with densities down to less than  $10 \text{ cm}^{-3}$ .

Besides the different plasma regions we were able to compare inferred dust characteristics of two independent instruments, both part of the RPWS. The main result is, that the dust is part of the collective behavior and needs to be treated as such in simulations.



The dust density follows a power law (Kurth et al., 2006; Kempf et al., 2008) and can be written in the following form

$$n_d(r_d) \propto r_d^{-\mu}, \mu \approx 4 - 5, \quad (6.1)$$

where  $n_d$  and  $r_d$  are the dust density and dust grain size. Using the expression for the capacitance of a sphere, we can estimate the grain charge in equilibrium with the surrounding plasma as

$$q_d = -\alpha 4\pi\epsilon_0 r_d \Phi_f \quad (6.2)$$

where  $q_d$  and  $r_d$  are the dust charge and size,  $\epsilon_0$  vacuum permittivity,  $\alpha$  a proportionality factor which is a function of the ion mass  $m_i$  and is about 3.66 for water group ions (Horányi et al., 2004; Shafiq et al., 2011), and  $\Phi_f$  the grain surface potential which can be approximated by the spacecraft potential,  $U_{SC}$ .

We can find an equation that relates two independently measured dust densities (see section 3.2). The differential density,  $n_i - n_e$ , and the total dust density for particles larger than  $1 \mu\text{m}$ ,  $n_{d,\text{tot}}$  (marked red)

$$n_i - n_e = - \left( \frac{4\pi\epsilon_0\alpha U_{SC}}{e} \right) \frac{(1-\mu)}{(2-\mu)} r_1^{\mu-1} \frac{1}{r_{\min}^{\mu-2}} n_{d,\text{tot}}(> r_1) \quad (6.3)$$

relating

$$n_i - n_e \propto n_{d,\text{tot}}(> r_1). \quad (6.4)$$

Figure 12 of article 1 (fig. 6.2 in here), shows a linear relation, as predicted by the equations. On the vertical axis is the dust density as gathered by Langmuir probe sweeps of electron and ion density, and the horizontal axis is the dust density of particles larger than  $1 \mu\text{m}$  as deduced by direct dust hits with the Wide Band Receiver. This shows, that the charged dust is in equilibrium with the surrounding plasma, and verifies the method of inferring charged dust from LP observations of ion and electron density. From this we can then infer the minimum dust particle size (marked blue in eq. (6.3)). This then results in a size down to 1 nm in the plume region, and down to 10 nm in both the plume edge and trail. This is consistent with studies by Wahlund et al. (2009); Shafiq et al. (2011) that infer small grains down to nm in size.

### Contribution

I performed the RPWS/LP and MAG data analysis and had the main responsibility for the article.

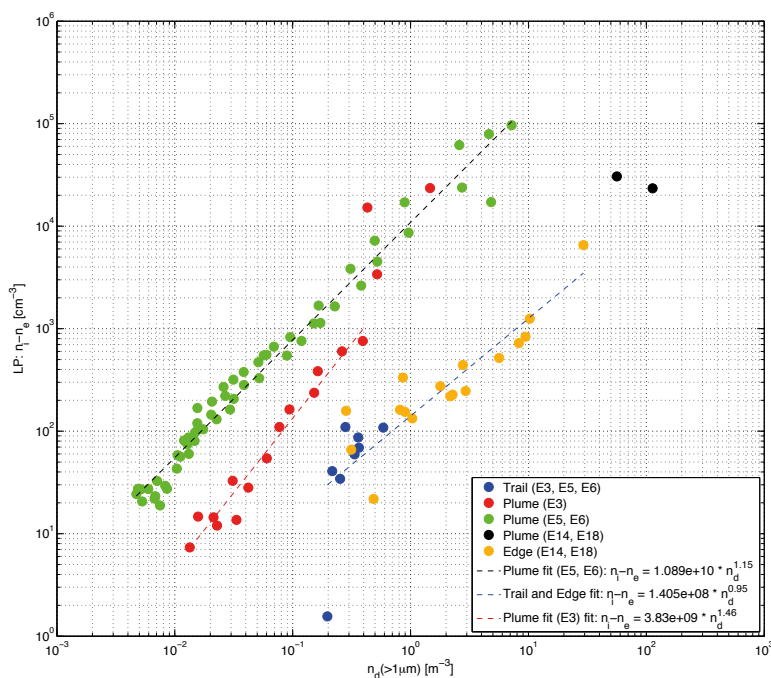


Figure 6.2: Charged dust density ( $n_i - n_e$ ) dependence on dust density of particles  $> 1 \mu\text{m}$ . The data is separated into the different regions. The plume is represented with data from the high inclination flybys E3 (red) and E5 and E6 (green) as well as E14 (left-) and E18 (right black data point). The trail (blue) is determined by flybys E3, E5 and E6, and the plume edge region (orange) by E14 and E18. The fit to the plume edge and trail, and the plume data shows an approximate linear relationship. Reused from Engelhardt et al. (2015, Figure 12), with permission from Elsevier.



# 67P/Churyumov-Gerasimenko

|           |                                                  |           |
|-----------|--------------------------------------------------|-----------|
| <b>7</b>  | <b>Rosetta - Mission and Instruments</b> . . . . | <b>41</b> |
| 7.1       | Mission                                          |           |
| 7.2       | Instruments                                      |           |
| <b>8</b>  | <b>Comet Environment</b> . . . . .               | <b>49</b> |
| 8.1       | Comet Plasma Physics (Pre-Rosetta)               |           |
| 8.2       | Updates from Rosetta                             |           |
| <b>9</b>  | <b>Article 2</b> . . . . .                       | <b>63</b> |
| <b>10</b> | <b>Article 3</b> . . . . .                       | <b>67</b> |
| <b>11</b> | <b>Article 4</b> . . . . .                       | <b>71</b> |





## 7. Rosetta - Mission and Instruments

### 7.1 Mission

Rosetta is a mission to study the comet 67P/Churyumov-Gerasimenko, hereafter called 67P. Rosetta met up with the comet and orbited close around it. The Rosetta spacecraft was launched into space in 2004 and arrived at the comet 10 years later. It carried the lander Philae which landed on the nucleus November 12, 2014, to directly study the nucleus surface in situ. Rosetta then continued to orbit the comet for another 2 years until on September 30, 2016, it was gently crashed on to the nucleus. The main mission objectives is to study the comet nucleus, its origin and the early solar system. It also provides the opportunity to study the structure and evolution of the cometary coma, which is the topic of this thesis.

The exact orbit of the Rosetta mission at the nucleus was dependent on the outgassing activity of the comet. The timeline is tabulated in table 7.1. Most of the time was spent as close as possible to the nucleus, to get detailed images, and sniffing traces of rare gases, but there were also two excursions to larger distances. "As close as possible" meant in practice as much as a few hundred km around perihelion in summer and early autumn 2015, and down to a few kilometers during the last months of the mission when the activity had decreased again.

The main discoveries, related to this thesis, up to the writing thereof, are summarized in chapter 8. In the following section is a short overview of Rosetta instruments.

| Date [dd-mm-yyyy] | Description                  |
|-------------------|------------------------------|
| 03-2004           | Launch                       |
| 03-2005           | First Earth gravity assist   |
| 02-2007           | Mars gravity assist          |
| 11-2007           | Second Earth gravity assist  |
| 05-09-2008        | Asteroid Steins flyby        |
| 11-2009           | Third Earth gravity assist   |
| 10-07-2010        | Asteroid Lutetia flyby       |
| 07-2011           | Enter deep space hibernation |
| 20-01-2014        | Wake-up from hibernation     |
| 05-2014           | Comet rendezvous maneuver    |
| 08-2014           | Global mapping of the comet  |
| 12-11-2014        | Lander delivery              |
| 13-08-2015        | Perihelion passage           |
| 12-2015           | Nominal Mission end          |
| 30-09-2016        | Extended Mission end         |

Table 7.1: Rosetta-Philae timeline

## 7.2 Instruments

The whole Rosetta mission carries 21 instrument groups, of them are 10 situated on the lander Philae, see tables 7.2 and 7.3 for a list. The instruments mainly used here are part of the Rosetta Plasma Consortium (RPC) instrument package. These are further described in the following section. Furthermore we use data from ROSINA (Rosetta Orbiter Spectrometer for Ion and Neutral Analysis).

### 7.2.1 RPC - Rosetta Plasma Consortium

The RPC is a joint plasma investigation instrument group that includes several different plasma instruments. These include an Ion Composition Analyzer (ICA), Ion and Electron Sensor (IES), Magnetometer (MAG), Mutual Impedance Probe (MIP), LAP, with a common interface to the spacecraft by the Plasma Interface Unit (PIU), see fig. 7.1.

| Acronym | Full Name                                                   |
|---------|-------------------------------------------------------------|
| ALICE   | Ultraviolet Imaging Spectrometer                            |
| CONSERT | Comet Nucleus Sounding Experiment by Radiowave Transmission |
| COSIMA  | Cometary Secondary Ion Mass Analyzer                        |
| GIADA   | Grain Impact Analyzer and Dust Accumulator                  |
| MIDAS   | Micro-Imaging Dust Analysis System                          |
| MIRO    | Microwave Instrument for the Rosetta Orbiter                |
| OSIRIS  | Optical, Spectroscopic and Infrared Remote Imaging System   |
| ROSINA  | Rosetta Orbiter Spectrometer for Ion and Neutral Analysis   |
| RPC     | Rosetta Plasma Consortium                                   |
| RSI     | Radio Science Investigation                                 |
| VIRTIS  | Visible and Infrared Thermal Imaging Spectrometer           |

Table 7.2: List of the 11 instrument groups on board Rosetta.

| Acronym | Full Name                                                                                            |
|---------|------------------------------------------------------------------------------------------------------|
| APSX    | Alpha Particle X-ray Spectrometer                                                                    |
| ČIVA    | Comet Infrared and Visible Analyzer                                                                  |
| CONSERT | Comet Nucleus Sounding Experiment by Radiowave Transmission                                          |
| COSAC   | Cometary Sampling Composition                                                                        |
| MODULUS | Methods Of Determining and Understanding Light Elements from Unequivocal Stable isotope compositions |
| MUPUS   | Multi Purpose Sensors for Surface and Subsurface Science                                             |
| ROLIS   | Rosetta Lander Imaging System                                                                        |
| ROMAP   | Rosetta Lander Magnetometer and Plasma Monitor                                                       |
| SD2     | Sample, Drill and Distribution                                                                       |
| SESAME  | Surface Electrical, Seismic and Acoustic Monitoring Experiments                                      |

Table 7.3: List of the 10 instrument groups on board the Philae lander.



In the next section follows a short introduction to the used instruments <sup>1</sup>.

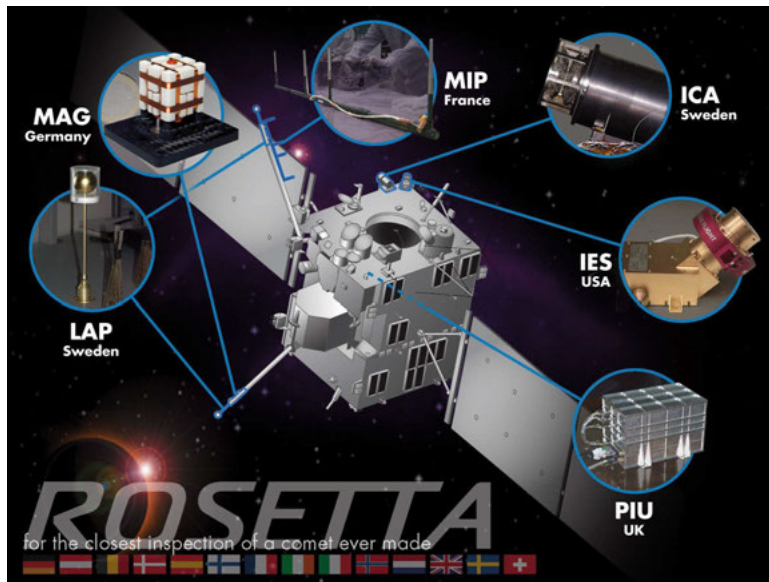


Figure 7.1: A picture of the Rosetta Plasma Consortium instruments on the Rosetta Spacecraft. Credits: STFC/Imperial College London

### 7.2.1.1 Langmuir probe

The Langmuir probe instrument, fig. 7.2, provided and operated by the IRF-Uppsala, consists of two separate Langmuir probes, known as LAP1 and LAP2 or just P1 and P2, and associated electronics. Both are identical and can be operated in different modes. They are mounted on 2.2 and 1.6 m long booms and the probes are separated by a distance of 5 m. There are different operation modes active during the mission, depending on the plasma characteristics. Main modes include: potential sweep, set bias potential, set current, floating probe, one probe aiding MIP measurements and for both probes together an e-field mode, see Eriksson et al. (2007) for more details.

The operational modes are defined by "macros", which are short programs run by the instrument. Each macro defines a sequence of measurements which is run over and over until another macro is commanded. The macros define which of the above measurement modes the probes are set to, and also how the data is downsampled to fit the available data transfer rate. There are two such rates, normal mode (NM, LAP data rate 55 bits/s) and burst mode (BM, 2200 bits/s), some macros being for normal mode and other for burst mode. Some macros

<sup>1</sup>The short description of RPC instruments is based on the information found on <http://sci.esa.int/rosetta/35061-instruments/?fbbodylongid=1644> and links therein.

were available at the start of the mission, while others were designed during the mission and uploaded to the instrument in response to changing plasma conditions.



Figure 7.2: One of the Langmuir probes on Rosetta. As for Cassini LP, the probe diameter is 5 cm, and the material is titanium with a coating of titanium nitride.

### 7.2.1.2 Ion Composition Analyzer

ICA was provided and operated by IRF-Kiruna. It measured positive ions. It can resolve solar wind protons, helium, water group ions and heavy ions that are characteristic to dusty plasma. ICA is also able to infer the spacecraft potential when it is negative (Odelstad et al., 2017). In this case all ions reaching the detector will have been accelerated through the spacecraft potential on their way in from the plasma, so one can find this potential as a lower cutoff in the energy spectrum. See Nilsson et al. (2007) for more details.

### 7.2.1.3 Mutual Impedance Probe

The MIP is provided by Centre National d'Études Spatiales (CNES). It primarily measures plasma density, although there is some capability to also infer electron temperature and drift velocity. MIP can also measure natural plasma waves above 7 kHz.

MIP consists of a rod with different transmitting and receiving dipole antennas at different distances from each other. The plasma characteristics are measured by the frequency response of a transmitted frequency. In particular, there will be a sharp spectral peak at the plasma resonance, whose frequency is the plasma frequency which only depends on electron density. The natural plasma waves however are measured when there is no frequency emitted. See Trotignon et al. (2007) for more information.

#### **7.2.1.4 Magnetometer**


The magnetometer instrument (MAG) on Rosetta consists of two tri-axial flux-gate magnetometers. They are situated on the same 1.6 m boom as LAP probe 2, one close to the end and one part way through. The use of two magnetometers (here we mean as magnetometer the tri-axial set of magnetometers) aids the subtraction of the spacecraft's own magnetic field, which is a large source of disturbance. See Glassmeier et al. (2007) for more information.

### **7.2.2 ROSINA - Rosetta Orbiter Spectrometer for Ion and Neutral Analysis**

#### **7.2.2.1 COmetary Pressure Sensor**

The Rosetta Orbiter Spectrometer for Ion and Neutral Analysis (ROSINA) instrument group consists of two mass spectrometers and one COmetary Pressure Sensor (COPS) (Balsiger et al., 2007). COPS can determine the neutral gas density and also has some capability for measuring the flow velocity, although the derivation of the flow velocity has not been used much (Tzou, 2017). This sensor is the one that will be used in the studies. The mass spectrometers are utilized to determine the comet's atmospheric/ionospheric composition.





## 8. Comet Environment

### 8.1 Comet Plasma Physics (Pre-Rosetta)

In 2004 ESA sent a spacecraft named Rosetta towards comet 67P/Churyumov-Gerasimenko. Since its arrival in 2014 and the following two years of the mission, much has been found about this particular/specific comet. Rosetta collected two years of data typically at a few tens to a few hundreds of kilometer, distance. But, what was known/postulated before this mission? This section gives a very brief summary of pre-Rosetta thoughts on cometary plasma physics mainly based on Gombosi (2014); Meech (2017); de Pater & Lissauer (2010), with some new additions from 67P as needed. Rosetta specific results follow in section 8.2.

#### 8.1.1 General Background

Comets are usually faint objects in the night sky and only the brightest are visible to the naked eye. Over the last 2000 years, there were on average only two comets per century bright enough to be seen without advanced optical equipment. They looked like hairy stars which gave them their name comet, derived from Greek meaning ‘the hairy one’. Because of the scarcity in the night sky, they were considered bringer of bad omens. The earliest record of a comet sighting dates back to about 6000 BCE.

The cloud that is visible in the night sky is very large (thousands-millions of km) which has only a few km sized solid body in its center. Cometary nuclei are now known to be quite similar to asteroids, being chunks of leftover material at

the formation of the solar system. Asteroids are however dominated by rocky non-volatile material while comets also consist of a significant amount of ices that can sublime when sufficiently heated. The first modern theory of comets can be said to be Whipple's (1950) "dirty snowball" hypothesis, according to which cometary nuclei are kilometer sized blocks of water ice and various compounds. While the elements of this hypothesis have been verified, it has been realized that "icy dirt balls" may be a better description as non-volatile material apparently dominate every investigated comet.

The first close up of a comet nucleus, 1P/Halley, in 1986 came from the Soviet spacecraft Vega 1. A few months later it was also visited by the European Giotto mission (ESA). These images showed that the nucleus had a complex shape with active regions, craters, valleys, hills, ridges and more. It was very dark (very low albedo of only 4%). It had a thick layer of dust and spots and cracks emanating gas and was overall very inhomogeneous. Similar results have been shown by other spacecraft passing by nuclei, eg. Stardust at 81P/Wild, Deep Impact at 9P/Tempel and EPOXI at 103P/Hartley.

Comets have formed far away from the Sun, however still in the solar system. They are considered to be icy planetesimals left over after planetary growth as relatively pristine objects from the early solar system that can give insight to the formation process of planets. Two main cometary reservoirs are recognized. These are the Oort cloud and the Kuiper Belt including the scattered disc. These reservoirs have been found by studying the orbits of comets. The Oort cloud has been estimated to host about  $10^{11} - 10^{12}$  comets. It is divided into an inner cloud and outer cloud. The inner cloud is situated at  $10^3 - 10^4$  AU while the outer, or the classical cloud, is situated at about  $> 10^4$  AU. The comets in the reservoir may enter the solar system when their orbit gets perturbed, making them dynamically new comets. The Kuiper belt is a region beyond the orbit of Neptune ( $R_{\Psi} \sim 30$  to 50 AU).

Comets are classified by their orbit. Short period comets are comets that have a period of less than 200 years and are also situated in the same plane and direction as the planets as expected for Kuiper belt objects. Long period comets however can have tilted orbits, which can be expected for comets originating in the Oort cloud. Only short period comets have been visited by spacecraft. They are easier to reach with spacecraft because they move close to the ecliptic plane and not as fast as the long period comets.

### 8.1.2 Comet Atmosphere and Coma

When the comet is at aphelion, far away from the Sun, it resides in a very cold environment. Kepler's second law (conservation of angular momentum) describes that a line connected from the Sun to the object on an elliptical orbit sweeps out the same area per time along the orbit, so the comet spends most of the time around the cold half of the orbit. As it however closes in to the Sun, it starts to heat up and the ices in the uppermost layers sublime into gas, creating a cometary atmosphere. The pressure of the created gas is very low to Earth standards but is much higher than the pressure of the surrounding space, which is assumed to be empty. The pressure gradient then drives the expansion of the cometary gas.

As the neutral gas exits the surface, it drags along loose dust. As a comet nucleus is small, with escape velocity on the order of 1 m/s, essentially all molecules and also many dust grains escape the comet. This gas and dust cloud, called the coma, can be seen by the naked eye. The coma typically is about  $10^4 - 10^5$  km in size.

The gas production rate,  $Q$ , assuming the neutral gas velocity is not zero ( $u \neq 0$ ), is given by:

$$Q = \oint n_n \vec{u} \cdot d\vec{S}. \quad (8.1)$$

where we assume that the nucleus is the only source of the gas.  $Q$  is measured in molecules/second. If we assume the outgassing is spherically symmetric we get

$$Q = 4\pi r^2 n_n(r) u(r). \quad (8.2)$$

This then gives the neutral gas density to be

$$\Rightarrow n_n(r) = \frac{Q}{4\pi r^2 u(r)}. \quad (8.3)$$

Numerical simulations of the gas molecular motion indicates that outside 10 km, the gas flow is radial and at constant velocity (Tenishev et al., 2008). With constant  $u$ , the neutral gas density profile can be approximated as

$$n_n \propto \frac{1}{r^2}. \quad (8.4)$$

The most common molecule in the coma usually is water,  $H_2O$ , although other species are often abundant, in particular  $CO_2$  and  $CO$ . A surprise from Rosetta was that also  $O_2$  turned out to be very common, sometimes reaching around or above 10 % (Bieler et al., 2015a). For the following, we will not have to care about the detailed chemistry and assume water dominates.



### 8.1.3 Comet Ionosphere

The gases are neutral as they are released from the volatile ices, however they get ionized and create an ionosphere. In the inner coma, the ionization process is dominated by direct photoionization and by impact of electrons accelerated to tens and hundreds of eV by the comet-solar wind interaction (Vigren et al., 2016; Galand et al., 2016; Heritier et al., 2017). Further out in the coma, charge exchange with solar wind ions also becomes important (Simon Wedlund et al., 2016).

The plasma is created by the ionization of the neutral gas and lost by recombination and transport. This is then described by the continuity equation

$$\frac{\partial n}{\partial t} + \nabla \cdot (n\vec{v}) = S - L \quad (8.5)$$

where  $n$  is the plasma number density,  $t$  the time and  $\vec{v}$  the ion velocity. The main plasma source,  $S$ , is then mainly ionization processes by the solar EUV and by electron impact with an energy higher than the ionization energy of the gas molecules, typically  $\gtrsim 10$  eV. This can be described by the effective ionization frequency,  $\vartheta$ , times the neutral density, so  $S = \vartheta n_n(r)$ . The main loss for the plasma,  $L$ , is by dissociative recombination ( $M_2^+ + e^- \rightarrow M + M$ , where  $M$  denotes a molecule and  $e^-$  an electron), which is proportional to the square of the plasma density,  $\propto n^2$ , and therefore important only in highly active comets or close to the nucleus. At 67P it is important only close to the nucleus around perihelion, so we will set  $L = 0$  (Vigren et al., 2016; Galand et al., 2016).

Assuming steady state,  $\partial/\partial t = 0$ , spherical symmetry so that  $\vec{v} = v\hat{r}$  and  $\nabla = \hat{r} \frac{\partial}{\partial r}$ , and a constant ion velocity,  $v$ , we get

$$\frac{1}{r^2} \frac{d}{dr} (r^2 n(r)) v = S - L \quad (8.6)$$

$$= \vartheta n_n \quad (8.7)$$

$$= \vartheta \frac{Q}{4\pi u r^2}. \quad (8.8)$$

Integrating this then gives the plasma density to be

$$n = \frac{\vartheta Q}{4\pi u v} \frac{1}{r} \left( 1 - \frac{R}{r} \right). \quad (8.9)$$

where we set  $n(R) = 0$ , since no molecules should be ionized when they leave the nucleus.  $R$  denotes the radius of the nucleus. Because there are collisions, the ion velocity,  $v$ , should be equal to the neutral gas velocity,  $u$  at least for highly active comets like 1P/Halley at perihelion. In the limit at far distances,



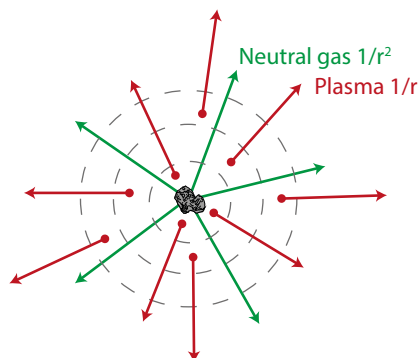


Figure 8.1: Visualisation of the neutral gas and plasma density decay. The neutral gas density decays with  $1/r^2$  while the plasma density decays as  $1/r$ . The neutral gas is represented by the green arrows, starting at the nucleus. Because  $S$  in eq. (8.5) decays with  $1/r^2$  and equally many ions are created in each spherical shell of the same thickness. In the figure 3 ions are created (red dots) that move approximately radially outward. The comet sketch comes from [https://commons.wikimedia.org/wiki/File:Comet\\_P67\\_Mark.svg](https://commons.wikimedia.org/wiki/File:Comet_P67_Mark.svg).

we thus expect to have

$$\lim_{r \rightarrow \infty} n \propto \frac{1}{r}. \quad (8.10)$$

In summary, the neutral gas density decays as  $1/r^2$  while the plasma density as  $1/r$ , see fig. 8.1

The probability that a neutral has been ionized in time  $t$  is given by  $\vartheta t$ , for  $t \ll 1/\vartheta$ . At 1.25 AU, the solar EUV ionization frequency for  $\text{H}_2\text{O}$  is about  $3 \cdot 10^{-7} \text{s}^{-1}$  (Vigren & Galand, 2013) so a typical value for the Rosetta mission can be set as  $10^{-7} \text{s}^{-1}$ . A molecule at distance  $r$  will have spent a time  $t = r/u$  in space, so the degree of ionization is given by

$$\frac{n}{n_n} \sim \vartheta \frac{r}{u}. \quad (8.11)$$

As an example, for comet 67P, at 100 km distance with a gas flow speed of 1 km/s the degree of ionization is approximately  $10^{-5}$ . This low degree of ionization means we can neglect feedback from the plasma to the neutral gas dynamics.

The neutral gas density here, eq. (8.3), does not include that neutrals are lost by ionization. To include this, one should follow the Haser profile (Haser, 1957).

This then is described as

$$n_n(r) = \frac{Qe^{-\vartheta r/u}}{4\pi r^2 u}. \quad (8.12)$$

Close to the comet,  $r \ll u/\vartheta$  and  $\exp(-\vartheta r/u) \rightarrow 1$  and in this limit eq. (8.3) is valid. Calculating this for 67P with  $u \sim 1$  km/s and  $\vartheta \sim 10^{-7}$ ,  $u/\vartheta \sim 10^7$  km and so the word "close" would mean about  $10^6$  km. This means, that eq. (8.3) is a good enough approximation in our case since Rosetta was never that far out. The disappearance of the neutral gas cloud by ionization is not important until 10 million km out ( $\sim 0.1$  AU).

But is the assumption that the ion velocity is constant correct? This has an effect on the theory as most assume that  $v = u$  (Vigren & Galand, 2013; Galand et al., 2016; Heritier et al., 2017). To find out what to expect, we will look at some energetics.

The velocity of a newly created electron is given by

$$v_e \sim \sqrt{\frac{2E}{m}} \quad (8.13)$$

which gives a velocity of  $\sim 1000$  km/s for a  $\sim 10$  eV electron. A newborn ion will have the velocity of the neutral gas since almost all of the excess energy goes to the lighter particle. Thus when the solar EUV ionizes a neutral, the electron velocity is much larger than the neutral gas velocity,  $v_e \gg u$ . The initial ion energy at a neutral gas velocity of 1 km/s is  $\frac{1}{2}mu^2 = 0.1$  eV, for water group ions ( $m \approx 20$  amu).

If nothing else interferes, the combination of the effect of a very fast electron and the gradient in the density results in that many more electrons than ions would leave the coma, which would be against quasi neutrality of a plasma. This is counteracted by the formation of an ambipolar electric field. The equation of motion of the electron gas is given by

$$m_e n_e \frac{d\vec{v}_e}{dt} = -\nabla p_e - en_e \vec{E} \quad (8.14)$$

where  $m_e$  is the electron mass,  $n_e$  the density and the pressure  $p_e = n_e k T_e$  by the ideal gas law, where  $T_e$  is the electron temperature. In equilibrium ( $\frac{d\vec{v}_e}{dt} = 0$ ) the electric field then follows as

$$\vec{E} = -\frac{\nabla p_e}{en_e} \quad (8.15)$$

$$= -\frac{kT_e}{en_e} \nabla n_e \quad (8.16)$$

$$= -\frac{kT_e}{e} \nabla \ln(n_e) \quad (8.17)$$

using eq. (8.10), we can find that  $\nabla \ln(n_e) \sim \frac{1}{r}$  and so

$$E_{amb} = \frac{kT_e}{er} \quad (8.18)$$

is the ambipolar electric field which is needed so that ion and neutral gas have the same velocity. If there are no collisions, this field accelerates the ions outwards, but as  $kT_e \sim 10$  eV and  $\frac{1}{2}mu^2 \sim 0.1$  eV, it does so past the neutral gas velocity. We get  $v \gg u$  and so the assumption  $v = u$ , breaks down.

Two solutions to this problem are suggested. The first is effect of electron cooling: if the electrons are rapidly cooled down to the neutral temperature,  $T_n \sim 10^2$ , K  $\sim 0.01$  eV, then the ambipolar electric field is small. This however would require high neutral density,  $n_n$ . The second would be that the ions follow the neutral gas closely because of collisions. Both of these theories seem to work well for 1P/Halley but are much more unclear for 67P because of its much lower production rate.

The understanding of the ionosphere of a weak comet like 67P is still incomplete. For example, Vigren & Eriksson (2017) showed that even when taking collisions into account, a weak ambipolar field accelerates ions to several times  $u$ , while Vigren et al. (2016), Galand et al. (2016) and Heritier et al. (2017) get good agreement with observed plasma density using theories assuming  $v = u$ . Still our results in article 4 (chapter 11) suggest the ambipolar field is there, as all the cold electrons we see must have been held back by this field to have gotten the time to cool down.

### 8.1.4 Solar Wind Interaction

The comet is not only influenced by solar heating but also by solar wind. The solar wind is a stream of particles, protons, electrons as well as some heavier ions blowing almost radially out from the Sun and crossing the solar system at 200-800 km/s. The solar wind was postulated by L. Biermann in 1951 when observations of comets showed that the ion tail always points away from the Sun. The solar wind also carries a magnetic field with it that is frozen in to the plasma. This interplanetary magnetic field (IMF) interacts with the charged particles around the comet nucleus.

The outgassing activity of a comet is set by its sublimation of volatiles, with a certain gas production rate. A comet sufficiently far away from the Sun behaves like a rock in space without any coma, or tails, see for example fig. 8.2a. Sufficiently far away can be very far. When Rosetta arrived at 67P at 3.6 AU, it was already quite active and an ionospheric plasma could be seen (Yang et al., 2016). As the heliocentric distance decreases, the gas production rate increases. A highly developed comet interacts with the solar wind in the following way.

Plasma is a very good conductor and the electric field in the own frame of reference is nearly zero. This leaves:

$$\vec{E} + \vec{v} \times \vec{B} = 0 \quad (8.19)$$

and field lines are said to be frozen in to the plasma. The solar wind carries with it the IMF and when it comes close to the comet, it slows down. This slow down is a result of the solar EUV ionization of the comet gas that creates new charged particles which are accelerated ultimately to solar wind speed by the electric field given by eq. (8.19). So the solar wind slows down, when a new ion is created, by conservation of momentum. The rate of creation of new ions is largest closest to the comet nucleus and so the solar wind plasma slows down much more, closer to the nucleus. This leads to draping of the magnetic field. See for example fig. 8.2b. Since the magnetic field is frozen in to the plasma, the slow down of the solar wind close to the nucleus causes an increase of the magnetic field. The magnetic field can be above tens of nT while the IMF is typically a few nT.

While a number of plasma regions and boundaries were inferred to exist from brief flybys of other comets, only two boundaries are generally agreed upon. These are the bow shock and the diamagnetic cavity.

The bow shock is a result of the slowed down solar wind plasma and transitions from supersonic to subsonic. The diamagnetic cavity, whose boundary is sometimes called ionopause or contact surface, separates the purely cometary material from the mixture outside and there is no magnetic field,  $\vec{B} = 0$ , inside the cavity.

The plasma processes mentioned in section 8.1.3 are thought to be mostly valid inside the diamagnetic cavity because the theory used here does not include the magnetic field. Outside however things get more complex. Rosetta did cross the diamagnetic cavity at least 665 times, with a total duration of about 50 hours, but was mostly outside (Goetz et al., 2016a).

In addition to the diamagnetic cavity boundary and the bow shock, there exist mathematical boundaries that are defined as composition boundaries. One example is the cometopause, where the ion composition switches from mostly  $H^+$  of the solar wind to mostly cometary ions ( $H_2O^+$ ,  $H_3O^+$ ) (Mandt et al., 2016). Another example is the exobase or collisionopause discussed in the next section.

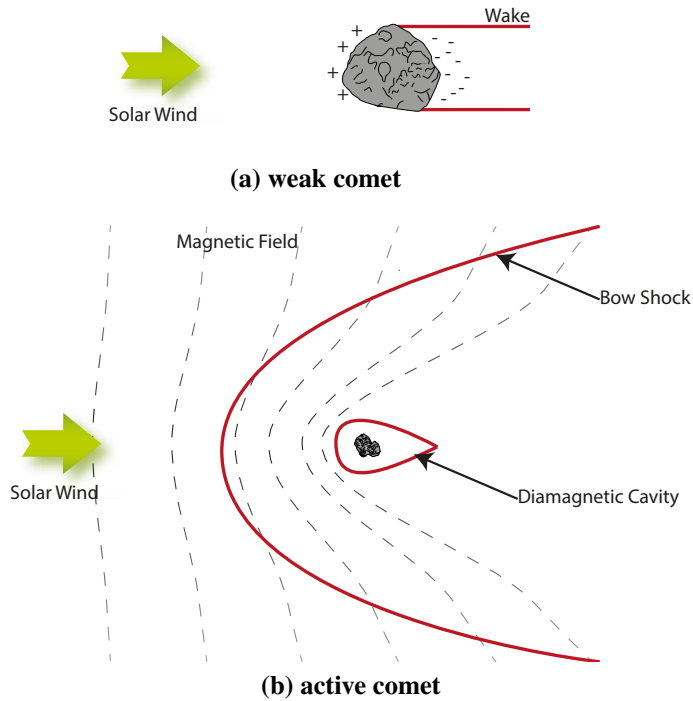


Figure 8.2: Boundaries of a weak (8.2a) and active (8.2b) comet. The weak comet gets charged directly by the solar wind creating a wake behind the nucleus. An active comet (high outgassing rate) develops a bow shock and diamagnetic cavity and causes draping of the solar wind magnetic field.

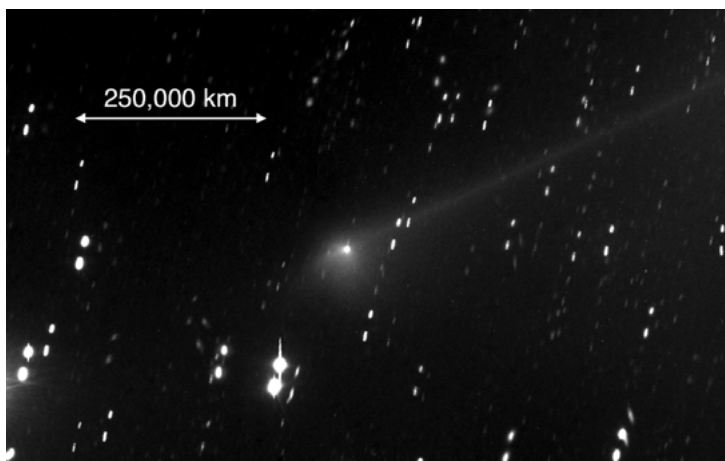


Figure 8.3: Image of 67P/C-G taken with the ESO VLT in April 2003, shortly after it was selected as the Rosetta target, when the comet was relatively close to the Sun. Image courtesy C. Snodgrass/ESO

## 8.2 Updates from Rosetta

One should always keep in mind, that everything we learned from Rosetta and 67P, comes from only one single example and is not necessarily the general truth for all comets, even of similar type. Nevertheless, Rosetta is the most detailed comet investigation ever, and the only in-situ study of how a comet evolves as its outgassing changes by 3 orders of magnitude ( $Q \sim 5 \cdot 10^{25} - 5 \cdot 10^{28} \text{ s}^{-1}$ ). The water production rate  $Q$  for 67P measured by Rosetta is shown in fig. 8.4. It changed by a factor 1000 during the Rosetta mission with the maximum just after perihelion. For comparison, the much more active comet C/1995 O1 Hale-Bopp reached a maximum of  $2 \cdot 10^{31} \text{ s}^{-1}$  at perihelion at 0.9 AU (Biver et al., 2002). Regarding the plasma environment, one can expect this mainly depends on the outgassing, so we can hope 67P is quite representative for low activity comets.

As previously mentioned, comet 67P is a Jupiter family comet with an orbital period of 6.45 years, a perihelion distance of 1.25 AU and aphelion distance of 5.68 AU. Shortly after 67P was selected as Rosetta's new target in 2003, the ESO/VLT caught a snapshot of the comet as it was 2.5 AU from the Sun, see fig. 8.3. It shows a developed coma and a very long tail.

The first surprise came immediately when we arrived at the comet. Instead of one big boulder, it looked like it was made up of two pieces, that represented the shape of a duck. The first question arose, if this is because two cometsimals collided with each other and stuck together, or if the comet was outgassing

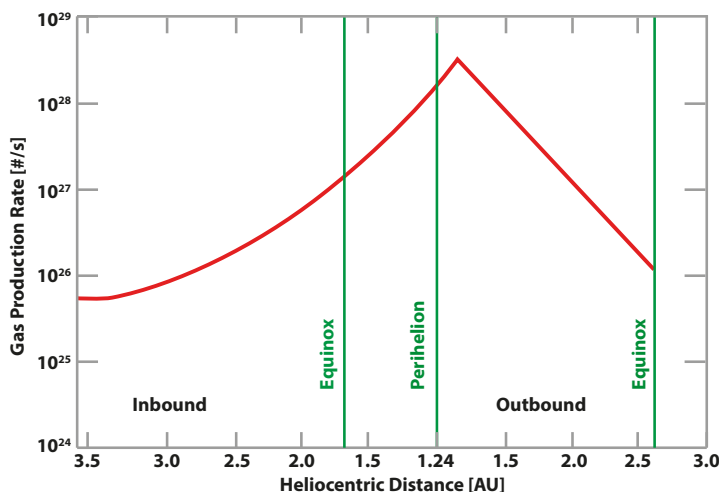


Figure 8.4: General trend of the water production rate of comet 67P during the Rosetta mission, based on Hansen et al. (2016, Fig. 6).

so unhomogeneously that the surface eroded more at the "neck" to form the shape. This question was later answered by Massironi et al. (2015). They could show that there are horizontal layer around each of the two parts of the nucleus, and that these go all around each of them, so they must have been created as two separate objects. Comparing to other comets, Borelly and Hartley 2 are shaped more like an elongated potato, but also these probably consist of two or more parts. The separate lobes are  $4.1 \times 3.3 \times 1.8$  km for the large body and  $2.6 \times 2.3 \times 1.8$  km for the head (Preusker, F. et al., 2017). This results in an approximate volume of  $18.7 \text{ km}^3$  and it has a mass of about  $9.9 \cdot 10^{12} \text{ kg}$  (Pätzold et al., 2016). For simplified calculations, we often approximate it with a sphere of radius 2 km. The rotation period was close to 12 hours but varied a little during the Rosetta mission (Keller et al., 2015)

As mentioned before, the heating of the comet defines the neutral gas emission due to ice sublimation. This gas then gets ionized mainly by photoionization and electron impact ionization (Vigren et al., 2016; Galand et al., 2016; Heritier et al., 2017). When an electron is newly created it has an energy of typically around 10 eV (Haberli et al., 1996; Vigren & Galand, 2013). Collisions with neutrals can cool down the electrons. Theory often assumes that the electron gas in the inner coma should be that of the neutral gas ( $T_e \sim T_n$ ) which is a few 100 K ( $\sim 0.01 \text{ eV}$ ) (Tenishev et al., 2008; Biver et al., 2015). This, to be effective, requires a high neutral density. 67P is less active than for example its sibling 1P/Halley. This results in a lower collision frequency since this means that the the neutral gas density is lower. Therefore warm electrons (5-10 eV)

dominate the electron gas. This can be seen from the spacecraft potential as it is mainly negative during the whole mission (-5 to -10V) (Odelstad et al., 2015, 2017). The presence of warm electrons has also been confirmed by MIP and IES instruments on Rosetta (Broiles et al. (e.g. 2016)). But as it turns out, cold electrons are also observed by LAP (Eriksson et al., 2017) and MIP (Gilet et al., 2017). These studies only showed a few observations. In article 4 in this thesis (chapter 11) we show that cold electrons are very common. Even though 67P is less active, collisional cooling is evidently still possible.

The electron exobase is the distance within which electrons are collisional and with this are able to cool. It is also called electron collisionopause or electron cooling boundary (Mandt et al., 2016; Eriksson et al., 2017; Henri et al., 2017). It is not a very sharp boundary but rather a characteristic scale length. It is defined as the distance to the comet where the electron mean free path is equal to the neutral gas density scale height. The neutral density varies with distance as  $1/r^2$  (eq. (8.4)) and plasma density as  $1/r$  (eq. (8.10)) so the scale height can be taken to be equal to  $r$ . Inside, the electrons colliding with neutrals lose a fraction of their energy. As the mean free path is  $1/(\sigma n_n)$ , the electron exobase distance  $L_c$  is given by

$$L_c = n_n \sigma r^2 \quad (8.20)$$

where  $r$  is the cometocentric distance,  $n_n$  the neutral density and  $\sigma = 5 \cdot 10^{20} \text{ m}^2$  the electron-neutral cross section for 5 eV electrons colliding with water molecules. It can be noted that as  $\sigma$  depends strongly on energy (Itikawa & Mason, 2005), the exobase is different for different energies. Furthermore, one single collision does not cool an electron down from  $\sim 10$  eV to  $\sim 0.01$  eV, so the exobase concept is not precise.

Here we define the dimensionless distance of the spacecraft position in units of  $L_c$

$$R^* = \frac{r}{L_c} = \frac{1}{n_n \sigma r}. \quad (8.21)$$

During most of the mission Rosetta is situated outside the exobase ( $R^* > 1$ ). This does not mean, that there are no collisions expected, only the chance of an electron actually colliding with a neutral is small at the position of Rosetta. However, a lot of cooling may go on closer to the nucleus where the neutral density is higher.

Another finding is that the plasma environment around 67P turns out to be quite unstable (Edberg et al., 2015; Stenberg Wieser et al., 2017). This was first shown by MAG by finding "singing comet waves" around 10-100 mHz with relatively high amplitude,  $dB/B \sim 1$  (Richter et al., 2015; Koenders et al.,



2016). These waves were mainly found at low activity stages. While there is this unstable plasma environment around 67P, inside the diamagnetic cavity it is much less disturbed (Goetz et al., 2016b; Henri et al., 2017). However, large density variations have also been observed there (Hajra et al., 2017). Many cavity observations are short, just a few minutes or even less. Henri et al. (2017) noted that the density inside cavity observations following each other closely is the same. They suggested this may happen by a central cavity forming finger-like structures stretching out into the surrounding magnetized plasma. They also showed that more cavity observations were made when Rosetta was close to the electron exobase. The hybrid simulations by Koenders et al. (2015) also show that the cavity is unstable. Filaments of cold dense plasma were seen in the simulations to leave the cavity and propagate outward. These are however not unmagnetized ( $B = 0$ ) like the cavity fingers suggested by Henri et al. (2017). We show in article 3 (chapter 10) that structures like the filaments in the hybrid simulations are also seen by Rosetta. How the short cavity observations should be explained is still discussed. That the cavity size seems to relate to the electron exobase points to that cold electrons may be important, so our report of cold electrons in article 4 (chapter 11) may also be of interest for cavity physics.



## 9. Article 2

### Cold and warm electrons at comet 67P/Churyumov-Gerasimenko

The article, entitled "Cold and warm electrons at 67P/Churyumov-Gerasimenko", has been published by Astronomy and Astrophysics (Eriksson et al., 2017). Here follows a short summary.

This paper presents general aspects of LAP measurements, particularly probe bias sweeps, and reports cold ( $< 0.1$  eV) electron gas at the comet. Such cold electrons have been long predicted, as collisional cooling on the neutral gas should be effective, at sufficiently high neutral gas density. From the point of view of this thesis, the main result is that the cold electrons often appear in LAP data as pulses of high current. We first tried to explain these as due to dust but now interpret them as filaments of cold plasma.

The current-voltage curve of the LAP measurements show specific key signatures during the mission, see figure 2 in the manuscript. These different regimes are:

**Tenuous Plasma** ( $n \lesssim 10^1 \text{cm}^{-3}$ ) small plasma electron flux, such as solar wind. Here the current-voltage curve is dominated by photoemission from the probe and collection from the photoelectron cloud surrounding the spacecraft. In this regime, the plasma density can not be extracted directly from the sweep, but can be estimated from the spacecraft potential.

**Intermediate Plasma** ( $10^1 \lesssim n \lesssim 10^3 \text{cm}^{-3}$ ) plasma electron flux overcoming the spacecraft photoemission and ion flux, with a temperature of about 1-10 eV. This is the most typical environment around 67P. Here it is possible to extract the plasma density from the sweep as well as with

current measured at a constant bias potential. In this region either one warm population ( $T_e = 5 - 10$  eV) is needed to fit the current-voltage characteristics, or two electron populations with different temperatures are needed, indicating that some electrons have experienced collisional cooling.

**Dense Plasma** ( $n \gtrsim 10^3 \text{ cm}^{-3}$ ) electron flux dominated by electrons with energy of the order of 10 eV as the spacecraft is still highly negative (around -10 V). However, a cold electron population of temperature possibly as low as that of the neutral gas (a few hundred Kelvin) is also needed to explain the sweeps.

LAP typically does probe bias sweeps every few minutes. In between these sweeps, the instrument sets the probes at some fixed bias potential, usually  $\pm 30$  V. In these measurements, we found pulses in the current that can be much larger than the background current, up to  $\sim 15 \mu\text{A}$  in the case of a positive probe.

Large pulses were first noticed on the day when Philae landed on the comet nucleus (Nov 2014), and then pretty much throughout the whole mission. The pulse detections are not uniformly distributed around the nucleus. When Rosetta was in the northern hemisphere during northern summer, the pulses were mainly detected around the neck region, which is also where the neutral gas and plasma density are highest in this period (Bieler et al., 2015b; Edberg et al., 2015, e.g.). This region was deemed the most active during northern summer. In general we find the pulses in about the same regions as where Odelstad et al. (2015) noted the highest plasma densities.

One obvious question is if these single pulses are due to dust hits. Thus far, the dust seems to have only little impact on the collective plasma. This is in contrast to the findings at Enceladus in the first article of this thesis, where the dust is a significant component of the plasma, see chapter 6. This may be due to the different environments of Enceladus and 67P.

We can rule out that separate pulses are single dust grain impacts, as there are simultaneous pulse detections in both probes. The two LAP probes are separated by 5 m (Eriksson et al., 2007). Furthermore, in contrast to the millisecond pulses due to dust hits seen on Cassini, the pulses observed turned out to vary in length from a few seconds to well over a minute. Another option is a dust cloud hitting the spacecraft. Since we simultaneously observe pulses in both electron and ion mode ( $V_b$  set at positive and negative potential) this would indicate that the cloud consists of both positively and negatively charged dust particles. This may be possible if the dust grains are of different character, however it is unlikely that this happens over a long time or large region. Furthermore, considerations of the likely charge on dust grains and the total charge contained

in a pulse shows that the pulses carry far too much charge to be well explained by dust grains. All this indicates that the pulses are due to local variability of the plasma density rather than dust effects. Larger detections in the electron current indicates that the pulses are mainly due to the low temperature electrons. However, not every pulse has a clear counter part in the other LAP sensor. Because the ion current is usually much smaller than the electron current, the signal to noise ratio is lower for the ions. In addition there may be wake effects such that a plasma cloud only reacts to one of the sensors.

This makes the nature of the pulses quite consistent with the plasma filaments in the hybrid simulations by Koenders et al. (2015). Three plots from that article are reproduced in fig. 9.1. Figure 9.1a shows the simulated plasma density around the nucleus in the  $\hat{x}$ - $\hat{z}$  plane, where  $\hat{x}$  is the solar wind direction and  $\hat{z}$  is perpendicular to the interplanetary magnetic field. Finger-like filaments of dense plasma are seen to detach from the diamagnetic cavity region, deep inside the inner coma, where electron cooling is efficient as the neutral density is high, and moves out into surrounding space. Figures 9.1b and 9.1c shows the time evolution of the plasma density and magnetic field, respectively, along a cut in the  $\hat{z}$ -direction (solar wind electric field). Taking for example  $z = 100$  km, we find pulses of ten times higher density passing by in a time varying from a few to a few tens of seconds. So the filaments turning up in the simulation are expected to give signatures similar to those we observe.

### **Contribution**

I was responsible for the part of the paper regarding the pulses, including all data analysis.

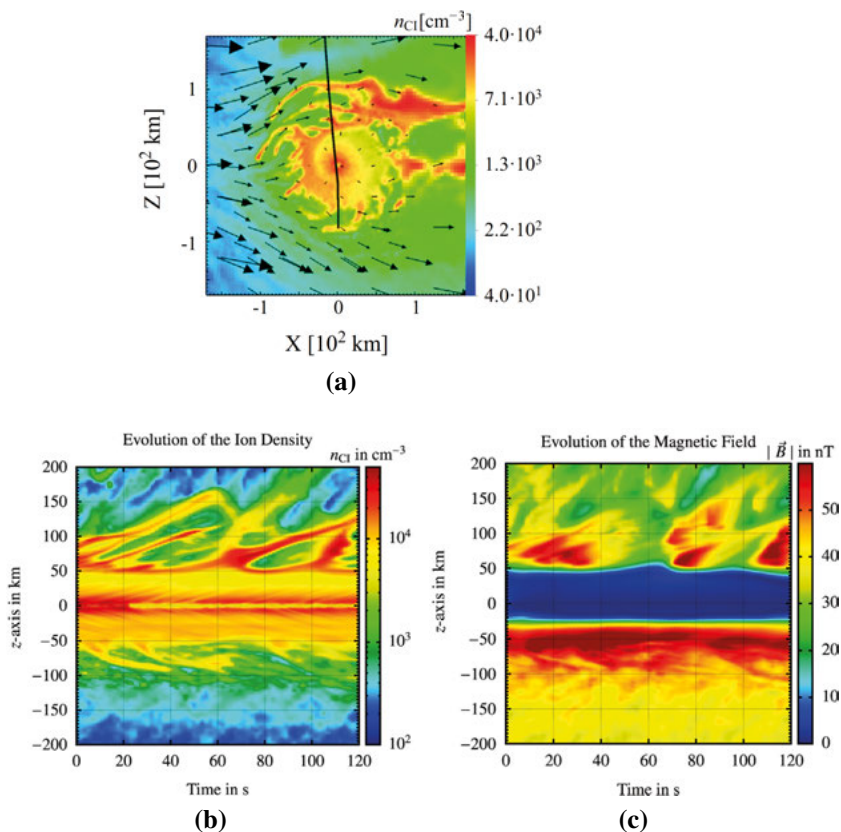


Figure 9.1: The solar wind flows in the  $+x$  direction, and the interplanetary magnetic field is in the  $x$ - $y$  plane. This is a hybrid simulation (ions are particles and electrons are fluid) with solar wind conditions typical for 1.3 AU and  $Q = 5 \cdot 10^{27} \text{ s}^{-1}$ . (a) shows density variations along  $x$  and  $z$ . Here small filaments can be seen. (b) and (c) show density and magnetic field variations in time, respectively. Looking along 100 km from the nucleus one sees pulses of various length in the density as well as magnetic field variations. Reused from (Koenders et al., 2015, Fig. 5e, 3c and 3d), with permission from Elsevier.

## 10. Article 3

### **Plasma density structures at 67P/Churyumov-Gerasimenko**

The article, entitled "Plasma density structures at 67P/Churyumov-Gerasimenko", has been published by Monthly Notices of the Royal Astronomical Society (Engelhardt et al., 2018). Here follows a short summary.

It builds on article 2, "Cold and warm electrons at 67P/Churyumov-Gerasimenko", see chapter 9. The goals here were to further understand the pulse nature by using data also from other RPC instruments and investigate their relation to electron cooling. This is an event study of LAP data and especially the cold plasma pulses therein. These are seen as sudden high amplitude spikes in the probe current that can last up to minutes in time.

We find that these kind of pulses can not only be seen in the plasma density measurements (LAP and MIP) but can also be seen in other RPC instruments, such as the ion energy flux (ICA) as well as the magnetic field measurements (MAG).

The dates for the four events are chosen from October and November 2015 and are all shortly after perihelion, August 13. They cover a variety of radial distance, phase angle and local time.

Here we make use of the derived electron density by MIP to calibrate the LAP data. The current measured by the Langmuir probe is proportional to the electron density (compare to section 2.2).

We have to assume the spacecraft potential, electron temperature and ion velocity stay constant over the time of calibration, since we do not have the data

in high time resolution. Doing this allows us to use a linear fit to the derived density by MIP.

$$n_{\text{MIP}} = A(I_{\text{LAP}} + B) \quad (10.1)$$

where  $A$  and  $B$  are the fitting parameters. Since in a plasma  $n_e \sim n_i$  we can use the same formula for both fitting electron and ion density.

For one of the events studied in this paper, the probe is set to measure the potential between the probes when no bias voltage or current is applied. Here we can use the approximation that the density is proportional to the spacecraft potential in the following way

$$n \propto \exp\left(-\alpha \frac{V_s}{T_e}\right). \quad (10.2)$$

This then turns into a linear fit of the logarithms

$$\log(n_{\text{MIP}}) = \log(D) + U_{\text{LAP}}/C \quad (10.3)$$

where  $C$  and  $D$  are the fitting parameters.

The fit itself is not perfect because of the assumptions of constant electron temperature and spacecraft potential, but it can give a good indication to compare the trend of these two independent measurements. The result is the same here as for the current measurements, verifying we can use either type of measurement to study these pulses.

Looking only at the two LAP probe signals, we see that pulses often coincide in time and amplitude, no matter if the probe is positively or negatively biased. So pulses can be seen simultaneously when both probes are set to electron mode (collecting electrons) or when both the electron and ion mode is used. This however can depend on the attitude of the spacecraft. If one of the probes is in the shadow of the Sun (either due to the spacecraft itself, the solar panels or the high gain antenna) the probes will show different currents. It might also be affected by the wake effect. Here the plasma outflow from the comet can get perturbed by the spacecraft.

When the plasma density is higher, the spacecraft potential is more negative (Odelstad et al., 2017). This can result in that the probe is not positive with respect to the plasma so that electrons can not be collected. This is especially problematic when the electrons are cold since they do not have enough energy to overcome the spacecraft potential. If however the probe is set to a negative potential, ions do more easily reach the probe when the spacecraft becomes more negative. Thus generally, when the plasma is dense, it is better to obtain the density from a negatively biased probe.



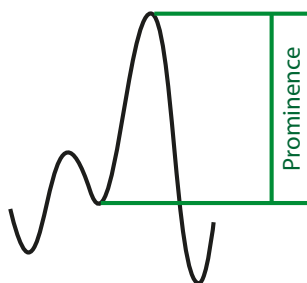


Figure 10.1: Example of the prominence of a peak. It is defined as the distance between a local maximum and the nearest minimum.

When looking at the other instruments, their variations do agree well with the pulses seen in LAP. This is another indication that these are local plasma variations. We furthermore included the neutral gas density data and used it to calculate the electron exobase distance to be able to quantify the plasma conditions further.

In this study, we also adjusted the algorithm for finding pulses, as compared to article 2 (chapter 9). It is now done with the new (2017) 'findpeaks' function provided by matlab. The algorithm looks for local maxima where the prominence is larger than a given threshold, here set to 20 nA. The prominence is defined as the height of the peak to the nearest local minimum. See as an example fig. 10.1.

The statistics were re-run on the ion current in LAP2 over the 2015 data from specific operational modes, where LAP2 was set to -17 V and -30 V respectively. These were then compared to the radial distance of Rosetta as well as the electron exobase distance. We can clearly see that when we are closer to the exobase, we detect more pulses.

We noted already in article 2 that the pulses could be plasma filaments from the diamagnetic cavity as seen in the simulations by Koenders et al. (2015). In this article we show that the pulses also are seen in the magnetic field, as is also the case in the simulations. Furthermore, we find them to be more common close to the exobase. Henri et al. (2017) showed that the main diamagnetic cavity seems to end around the exobase, so the pulses do also in this respect fit to the plasma filaments in the simulations.

### Contribution

I had the main responsibility for the paper, planned the work, selected events and did all data analyzes.



## 11. Article 4

### Cold electrons at comet 67P

The article, entitled "Cold electrons at comet 67P/Churyumov-Gerasimenko", has been submitted to *Astronomy and Astrophysics* (Engelhardt et al., 018b). Here follows a short summary.

As article 3, it builds on article 2, "Cold electrons at 67P/Churyumov-Gerasimenko", see chapter 9. This time however, the focus is on LAP observations of cold electrons in general.

Newly created electrons have energies of about 10 eV. Due to collision between electrons and neutrals, electrons can lose a fraction of their energy and cool down toward the neutral gas temperature. In this article we provide a method to identify cold electrons. For this, we show that the slope of the electron side of the Langmuir probe sweep can be used to identify cold electrons.

As mentioned in section 2.2 the electron current to a positively charged Langmuir probe is given by

$$I = 4\pi a^2 n_e \sqrt{\frac{eT_e}{2\pi m_e}} \left(1 + \frac{U}{T_e}\right) \quad (11.1)$$

where  $T_e$  is given in eV and the slope at this side of the sweep is given by

$$S = \frac{dI}{dU} = a^2 e^{3/2} \sqrt{\frac{8\pi}{m_e}} \frac{n_e}{\sqrt{T_e}}. \quad (11.2)$$

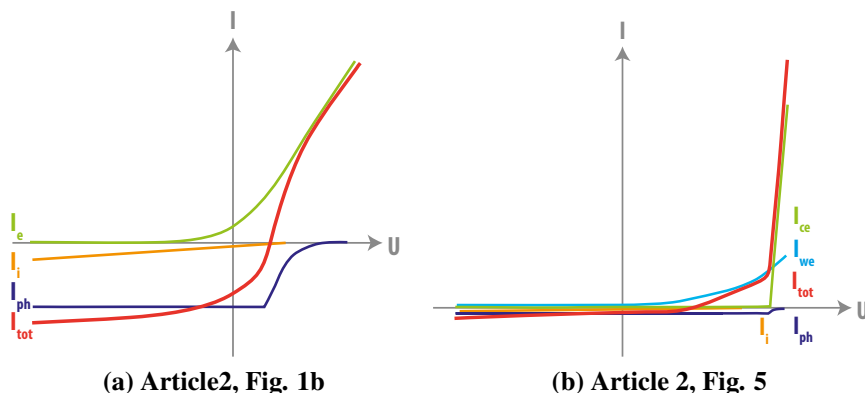


Figure 11.1: Two versions of a response to a Langmuir probe sweep, based on actual data from article 2, chapter 9.  $I_i$ ,  $I_e$ , and  $I_{ph}$  are the contributions from the ions, the electrons and the photoelectrons, and  $I_{ce}$  and  $I_{we}$  are the contribution of cold and warm electrons, respectively. Figure 11.1a shows the signature of expected response to a warm plasma while fig. 11.1b shows the response when cold electrons reach the probe. The slope on the electron side is much steeper than in 11.1a and  $I_{ce}$  dominates the slope at high potential.

A general shape of a LAP sweep is shown in fig. 11.1a. This slope is adapted from figure 1b in article 2. Figure 11.1b, on the other hand, shows a sweep with where at least 25% of the electrons are cold.

Using the slope of the Langmuir probe and the electron density from the Mutual Impedance Probe, we can estimate the temperature of the electrons as

$$T_s = 8\pi \frac{a^4 e^3}{m_e} \frac{n_e^2}{S^2}. \quad (11.3)$$

We can show, that the cold temperatures we measure, come exclusively from the steep slopes (figures 3 and 4 in the article) and less steep slopes are identified with larger temperatures. Temperatures, derived by this method, between 10 and 100 eV are to be taken with a grain of salt, and temperatures  $<100$  eV should be discarded as bad data.

Furthermore we show the statistics over the whole mission for when we see cold electrons. As it turns out, we see them early on in the mission, when the comet was not so active, until almost the end of mission. To see when we expect them, we consider the electron exobase, as explained in section 8.2. It is a gradual boundary inside where electrons are colliding with neutrals. For a region to exist where there is collisionality expected, the exobase distance needs to be

larger than the nucleus. Translating this to a time frame to predict when cold electrons are expected, we showed that this should be between March 2015 and March 2016 (article 4, Figure 1).

Another model is the continuous cooling model where the average energy lost due to collisions by an electron along the path is calculated. The underlying assumption is that these do move radially outward and do not divert from their path. This is of course a simplification, but with this we can calculate the energy as a function of distance for an electron moving outward from any given point in the coma. Here we include electron energy loss both by rotational and vibrational excitation of a water molecule. The cooling of the electron depends on the neutral gas density and the energy of an electron. The lower the electron energy, the quicker it loses energy to the neutral gas. The neutral gas density does decrease approximately with  $1/r^2$ . When doing these calculations for a newly created electron, at the nucleus, with an energy of 1 eV, we expect energy loss to a level below 0.2 eV as suggested by the existence of an exobase, approximately between March 2015 and March 2016. However, for a 10 eV electron this time frame is down to 1-2 months around perihelion. As most electrons are newly created in this energy range, we find cold electrons over a larger part of the mission than this model can explain.

The two simple models used here are not enough to explain the cold electrons during the whole mission. One mechanism that could keep electrons in the dense region, close to the nucleus, to cool down more efficiently, could be the ambipolar electric field (section 8.1.3).

There are two effects for how the ambipolar field can influence the cooling of electrons. The first effect is, that with this field, the electrons are kept inside the dense gas, close to the nucleus which gives them enough time to collide with neutrals more often and cool down. As its energy decreases, the energy loss becomes quicker. See fig. 11.2a as an illustration. The second effect of the field is, that the electrons are losing their kinetic energy to potential energy and are slowed down. See fig. 11.2b. The two effects together should be efficient for electron cooling and may explain why we see so much cold electrons despite the fact that 67P is not a very active comet.

### **Contribution**

I had the main responsibility for the paper and performed all data analysis. The theory in section 2.2 was contributed by the second author.

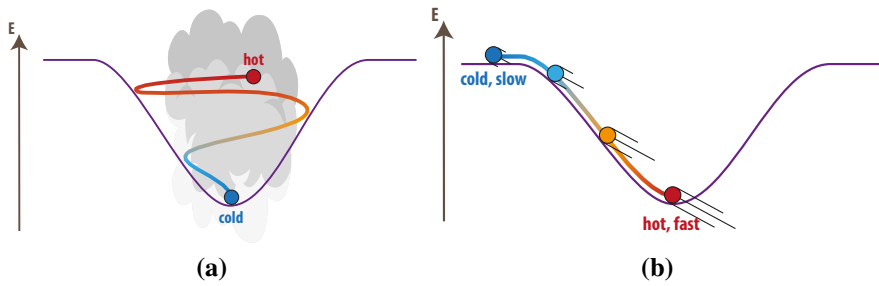


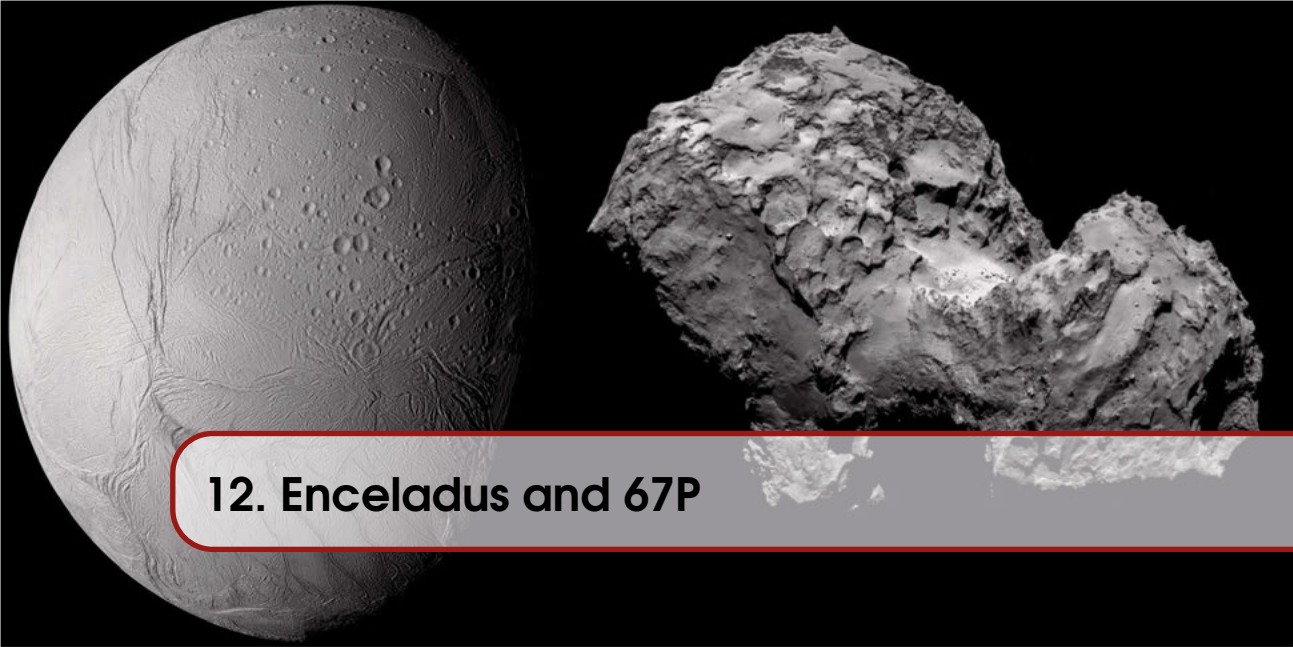
Figure 11.2: Ambipolar electric field effects on electrons. 11.2a Keeping the electrons close to the nucleus and 11.2b converting kinetic energy of an electron to potential energy.

# IV

## Coda







## 12. Enceladus and 67P

### Comparison

The main purpose of this research was to study the dust and plasma environment of the icy moon Enceladus and compare, or even use, it to quantify the dust and plasma environment of comet 67P/Churyumov-Gerasimenko. As it turns out, it is not as simple as hoped.

One most apparent similarity is that both objects spew out gas and dust, albeit through different processes. Enceladus has an under-ice ocean and water escapes as geysers through cracks in the ice. On comets there is no liquid water and gas escapes from sublimation at, or near the surface. Both outgassing compositions include water and water vapor. Another eminent similarity is the fact that the outgassing is structured and jets can be seen in the general expulsion from the object. The outgassing of both objects also drags along some dust.

One major difference is the shape of the object itself. Due to self gravity, the moon is nearly spherical. The comet on the other hand is usually oddly shaped and a clump of material, most probably stuck together by collision. Due to the self-gravity at the moon, it also can be more compact and not as porous as a comet. These differences were well known at the start of the project, but the space environments of the bodies could still be assumed to show some similarities.

One big difference is also the source of heat. At the comet, the solar radiation heats up the comet from which the surface sublimates while at the moon we have another internal source of heat. Boice & Goldstein (2009) tried to

use known comet physics to explain the outgassing and plasma physics of Enceladus. The similarities mentioned here are the emission of dust and gas as well as jet-like features in the plume or coma. The region of outgassing changes the characteristics of the surface as dust can accumulate. Another possible similar aspect is the heat and gas transport. While major differences are due to the effect of the gravity, density, liquid water source, cryovolcanism, internal inhomogeneities and a quasi-bound dusty atmosphere.

Other differences that could be relevant for the comparison of the plasma environments of Enceladus and 67P is the distance to the Sun as well as the different space plasma environment. The heliocentric distance differs by a factor 3-8 and the sunlight was 10-60 times stronger at 67P, when visited by Rosetta, than at Enceladus. Therefore photoionization at 67P is stronger. The surrounding environment differs by the strength of the magnetic field. The magnetic field of Saturn is about 330 nT at Enceladus, while the interplanetary magnetic field (IMF) is much weaker at 67P.

The biggest difference, relevant for this work is the dust. Due to different sources and expulsion mechanisms, the dust grains at Enceladus are very different from the dust at 67P. The dust grains are very small at Enceladus, in the nanometer size range (Hill et al., 2012, e.g.), while at 67P the dust is typically large, several millimeter or more (Rotundi et al., 2015; Della Corte et al., 2016; Merouane et al., 2016).

The size of the dust particles has a strong impact on the amount of electrons in a plasma that can get attached to the dust grains (see section 5.2, equation 17, of article 1). If there are more small dust grains, more electrons end up on the dust. In addition, if they are small, the charged dust grains are more influenced by electromagnetic forces. The dust-plasma interaction is much more important at Enceladus where much more electrons stick to dust grains, than at 67P. While Enceladus has more of a dusty plasma 67P seems to be more a dust-in-plasma case, as mentioned in section 3.1.

So, while the Enceladus study was mostly on dust-plasma physics, it was not at 67P. Actually, no dust-plasma interaction has yet been identified in the Rosetta data. This does not mean there is none, but further investigations are needed.


While the instruments on both spacecraft were similar, the conditions were different. There was for example no dust impact ionization at Rosetta since it moved at a much lower speed of about 1 m/s while Cassini passed by Enceladus on average with 9 km/s. At Cassini the ion ram current was approximately known and the spacecraft velocity was higher than the ion velocity ( $v_{s/c} \gg v_{ion}$ ) and at Rosetta this was not the case.



# Backmatter

|                        |    |
|------------------------|----|
| Swedish Summary .....  | 81 |
| Acknowledgements ..... | 83 |
| Acronyms .....         | 85 |
| Bibliography .....     | 87 |





## Swedish Summary

Saturnusmånen Enceladus och kometen 67P/Churyumov-Gerasimenko är två exempel på isiga objekt i solsystemet från vilka det strömmar ut gas och stoft i rymden. Vid båda himlakropparna blir gasen delvis joniserad och stoftkornen blir elektriskt laddade. Båda kropparna har besökts av rymdfarkoster försedda med Langmuirsondsinstrument för observationer av plasmat och det laddade stoftet. Det visar sig att förhållandena vid Enceladus och kometen skiljer sig åt, så vi uppmärksammar i denna avhandling olika aspekter av deras plasmaomgivning. Vid Enceladus koncentrerar vi oss på karakteristiska plasmaregioner samt det laddade stoftet. Vid kometen undersöker vi plasmat, framför allt plasmavariationer och förekomsten av kall elektrongas.

Enceladus värms upp inuti genom tidvattenkrafter från Saturnus. Uppvärmningen leder till gasutflöden genom sprickor i isen i området runt månens sydpol. Detta ger upphov till en gasplym som blir delvis joniserad. Stoftkorn som följer med gasen kan då laddas upp. Vi har undersökt plasmat och de laddade nanostoftet i detta område genom att använda Langmuirsonden LP inom Radio- och plasmavågsinstrumentet RPWS ombord på Cassini. Stoftets laddningstäthet kan beräknas från skillnaden mellan jongasens och elektrongasens laddningstätheter, eftersom total laddningstäthet måste vara nära noll (kvasineutralitet). Vi kunde visa att metoden ger resultat som väl följer mätningarna av större stoftkorn med RPWS radioantennerna. Med hjälp av LP-metoden kan vi visa att plasma- och stoftomgivningen runt Enceladus kan delas in i åtminstone tre regioner. Förutom den välkända plymen är dessa områden de som vi kallar för plymkanten (plume edge) och stoftspåret (dust trail).

Vid kometen får värme från solen isen att sublimeras till gas. Gasen drar med sig stoft när den flödar ut i rymden. När gasen joniseras av solens UV-strålning (fotojonisation) och kollisioner med högenergetiska elektroner (impaktjonisation) får vi ett plasma, på samma sätt som i Enceladusplymen. Modeller visar att elektrongasens temperatur strax efter jonisering är runt 10 eV (100 000 K), men att kollisioner med neutralgasens molekyler kan kyla ned elektronerna till under 0.1 eV (1000 K). Vi använde Langmuirsondinstrumentet LAP på Rosetta för att uppskatta elektrontemperaturer och visa att varm och kall elektrongas finns samtidigt i plasmat. De kalla elektronerna syns ofta som kortvariga pulser i data såväl från LAP som från i mätningar av magnetiskt fält, plasmatäthet och jonenergi med andra plasmainstrument på Rosetta. Vi tolkar pulserna som filament av plasma som rör sig utåt från den diamagnetiska kaviteten innerst i koma, som förutsagts av hybrid simuleringar. Gasproduktionen hos komet 67P varierade med mer än en faktor 1000 under Rosettas undersökningsperiod. Vi har därför en utmärkt och helt ny möjlighet att undersöka hur elektronkylningen i en kometes koma ändras med kometens aktivitet. Vi använder en metod där data från LAP och impedansprobinstrumentet MIP kombineras för att visa närvaron av kalla elektroner. Vi visar att de var synliga under en stor del av Rosettas undersökningar, och så långt ut i solsystemet som vid tre astronomiska enheter. Modeller antyder att kylningen borde vara försumbar på sådant långt avstånd från solen. Vi diskuterar möjligheten att ett ambipolär elektriskt fält håller kvar elektronerna nära kärnan så att de därmed får mer tid att förlora energi via kollisioner.



## Acknowledgements

Obviously, this thesis would not have been possible without the help and support of others.

In particular I would like to thank Anders Eriksson as my main supervisor, main proof reader of this thesis and papers, and the originator of the idea for the thesis. Also Jan-Erik Wahlund and David Andrews who helped me a lot with the first part of the research. Also thanks to Niklas Edberg and Erik Vigren who helped during both the first and the second parts. Thank you Mats André for making sure I stayed (or got back) on track.

Thanks also to the all engineers working hard to make the science projects work. A big thank you goes out to Sven-Erik Jansson for emergency repairing my soprano saxophone and Walter Puccio for saving my phone from drowning. Also Jenny Andersson, for the administrative support in keeping things smoothly.

Thank you Oleg Shebanits for sharing the office and Cassini knowledge, Elias Odelstad for the Rosetta/Matlab support.

Thank you Johanna 'Jojo' Rogvall for all the help with my sailing boat (Miss Bliss) and the nice 'get-aways'. I stayed in touch with the Netherlands through Stefanie Kooijman and Franciska Sathiady.

The biggest thanks goes to my family. Without the loving support from my parents Ralph and Dorothee I wouldn't have made it this far. Danke! Thanks also to my big brother André for all the technical help and Ann.

Last but not least, thank you to my partner, Mikael 'Årä' Grossman, for keeping me calm and laughing.

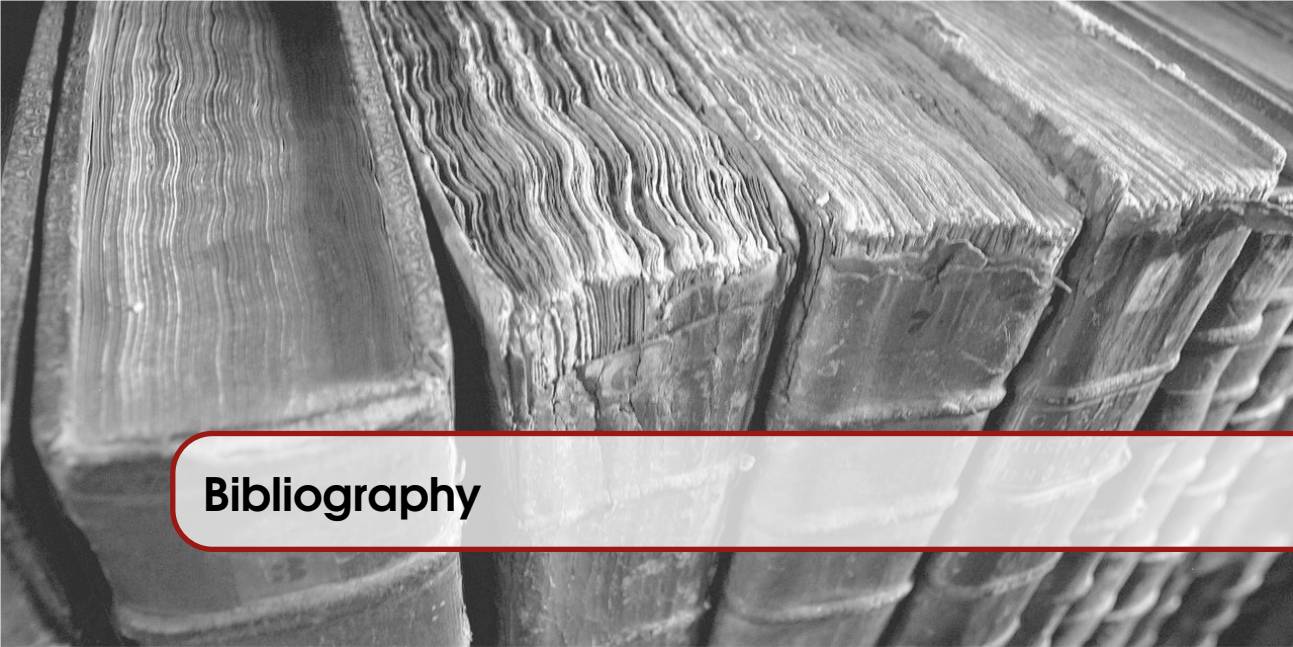






---

|                                                                                                                      |                                                                                |
|----------------------------------------------------------------------------------------------------------------------|--------------------------------------------------------------------------------|
| <b>LP</b> Langmuir probe.                                                                                            | <b>RADAR</b> Cassini Radar.                                                    |
| <b>MAG</b> Magnetometer.                                                                                             | <b>ROLIS</b> Rosetta Lander Imaging System.                                    |
| <b>MIDAS</b> Micro-Imaging Dust Analysis System.                                                                     | <b>ROMAP</b> Rosetta Lander Magnetometer and Plasma Monitor.                   |
| <b>MIMI</b> Magnetospheric Imaging Instrument.                                                                       | <b>ROSINA</b> Rosetta Orbiter Spectrometer for Ion and Neutral Analysis.       |
| <b>MIP</b> Mutual Impedance Probe.                                                                                   | <b>RPC</b> Rosetta Plasma Consortium.                                          |
| <b>MIRO</b> Microwave Instrument for the Rosetta Orbiter.                                                            | <b>RPWS</b> Radio and Plasma Wave Science.                                     |
| <b>MODULUS</b> Methods Of Determining and Understanding Light Elements from Unequivocal Stable isotope compositions. | <b>RSI</b> Radio Science Investigation.                                        |
| <b>MUPUS</b> Multi Purpose Sensors for Surface and Subsurface Science.                                               | <b>RSS</b> Radio Science System.                                               |
| <b>NASA</b> National Aeronautics and Space Administration.                                                           | <b>SD2</b> Sample, Drill and Distribution.                                     |
| <b>NM</b> normal mode.                                                                                               | <b>SESAME</b> Surface Electrical, Seismic and Acoustic Monitoring Experiments. |
| <b>OML</b> orbit motion limited.                                                                                     | <b>SSI</b> Surface Science Package.                                            |
| <b>OSIRIS</b> Optical, Spectroscopic and Infrared Remote Imaging System.                                             | <b>UVIS</b> Ultraviolet Imaging Spectrograph.                                  |
| <b>PIU</b> Plasma Interface Unit.                                                                                    | <b>VIMS</b> Visible and Infrared Mapping Spectrometer.                         |
|                                                                                                                      | <b>VIRTIS</b> Visible and Infrared Thermal Imaging Spectrometer.               |
|                                                                                                                      | <b>WBR</b> Wide Band Receiver.                                                 |



## Bibliography

- H. Balsiger, et al. (2007). 'Rosina – Rosetta Orbiter Spectrometer for Ion and Neutral Analysis'. *Space Science Reviews* **128**(1-4):745–801.
- A. Bieler, et al. (2015a). 'Abundant molecular oxygen in the coma of comet 67P/Churyumov–Gerasimenko'. *Nature* **526**:678–681.
- A. Bieler, et al. (2015b). 'Comparison of 3D kinetic and hydrodynamic models to ROSINA-COPS measurements of the neutral coma of 67P/Churyumov-Gerasimenko'. *Astronomy & Astrophysics - Special Feature* **583**:1–10.
- N. Biver, et al. (2002). 'The 1995–2002 Long-Term Monitoring of Comet C/1995 O1 (HALE-BOPP) at Radio Wavelength'. *Earth, Moon, and Planets* **90**:5–14.
- N. Biver, et al. (2015). 'Distribution of water around the nucleus of comet 67P/Churyumov-Gerasimenko at 3.4 AU from the Sun as seen by the MIRO instrument on Rosetta'. *Astronomy & Astrophysics - Special Feature* **583**:1–7.
- D. C. Boice & R. Goldstein (2009). 'A cometary perspective of Enceladus'. *Proceedings of the International Astronomical Union* **5**(Symposium S263):151–156.
- T. W. Broiles, et al. (2016). 'Characterizing cometary electrons with kappa distributions'. *Journal of Geophysical Research : Space Physics* **121**(8):7407–7422.
- M. H. Burger, et al. (2007). 'Understanding the escape of water from Enceladus'. *Journal of Geophysical Research* **112**(A6):A06219.
- T. Cravens, et al. (2009). 'Plume ionosphere of Enceladus as seen by the Cassini ion and neutral mass spectrometer'. *Geophysical Research Letters* **36**:L8106.

- I. de Pater & J. Lissauer (2010). *Planetary Sciences*. Cambridge University Press, Cambridge, 2 nd edn.
- V. Della Corte, et al. (2016). ‘67P/C-G inner coma dust properties from 2.2 au inbound to 2.0 au outbound to the Sun’. *Monthly Notices of the Royal Astronomical Society* **462**:S210–S219.
- Y. Dong, T. W. Hill, & S.-Y. Ye (2015). ‘Characteristics of ice grains in the Enceladus plume from Cassini observations’. *Journal of Geophysical Research: Space Physics* **120**(2):915–937.
- M. K. Dougherty, et al. (2006). ‘Identification of a Dynamic Atmosphere at Enceladus with the Cassini Magnetometer’. *Science* **311**(1406):1406–1409.
- N. J. T. Edberg, et al. (2015). ‘Spatial distribution of low-energy plasma around comet 67P/CG from Rosetta measurements’. *Geophysical Research Letters* **42**(11):4263–4269.
- I. A. D. Engelhardt, et al. (submitted, 2018b). ‘Cold electrons at 67P/Churyumov-Gerasimenko’. *Astronomy & Astrophysics*.
- I. A. D. Engelhardt, et al. (2015). ‘Plasma regions, charged dust and field-aligned currents near Enceladus’. *Planetary and Space Science* **117**:453–469.
- I. A. D. Engelhardt, et al. (2018). ‘Plasma density structures at comet 67P/Churyumov-Gerasimenko’. *Monthly Notices of the Royal Astronomical Society* **477**(1):1296–1307.
- E. Engwall (2006). *Cold magnetospheric plasma flows: Properties and interaction with spacecraft*. Licentiate thesis, Uppsala University.
- A. I. Eriksson, et al. (2007). ‘RPC-LAP: The Rosetta Langmuir Probe Instrument’. *Space Science Reviews* **128**:729–744.
- A. I. Eriksson, et al. (2017). ‘Cold and warm electrons at comet 67P/Churyumov-Gerasimenko’. *Astronomy & Astrophysics* **605**(A15).
- W. W. M. Farrell, et al. (2012). ‘The electromagnetic pickup of submicron-sized dust above Enceladus’s northern hemisphere’. *Icarus* **219**:498–501.
- B. L. Fleshman, P. a. Delamere, & F. Bagenal (2010). ‘Modeling the Enceladus plume-plasma interaction’. *Geophysical Research Letters* **37**:L03202.
- M. Galand, et al. (2016). ‘Ionospheric plasma of comet 67P probed by Rosetta at 3 au from the Sun’. *Monthly Notices of the Royal Astronomical Society* **462**:S331–S351.
- N. Gilet, et al. (2017). ‘Electrostatic Potential Radiated by a Pulsating Charge in a Two-Electron Temperature Plasma’. *Radio Science* **52**(11):1432–1448.
- K.-H. Glassmeier, et al. (2007). ‘The Rosetta Mission: Flying Towards the Origin of the Solar System’. *Space Science Reviews* **128**:1–21.

- C. Goetz, et al. (2016a). ‘Structure and evolution of the diamagnetic cavity at comet 67P/Churyumov–Gerasimenko’. *Monthly Notices of the Royal Astronomical Society* **462**(Suppl 1):S459–S467.
- C. Goetz, et al. (2016b). ‘First detection of a diamagnetic cavity at comet 67P/Churyumov–Gerasimenko’. *Astronomy & Astrophysics* **588**(A24):1–6.
- T. I. Gombosi (2014). ‘Physics of Cometary Magnetospheres’. *Magnetotails in the Solar System* pp. 169–188.
- R. Grard (1973). ‘Properties of the Satellite Photoelectron Sheath Derived from Photoemission Laboratory Measurements’. *Journal of Geophysical Research* **78**(16):2885–2906.
- D. Gurnett, et al. (1983). ‘Micron-sized particles detected near Saturn by the Voyager plasma wave instrument’. *Icarus* **53**(2):236–254.
- D. a. Gurnett, et al. (2011). ‘Auroral hiss, electron beams and standing Alfvén wave currents near Saturn’s moon Enceladus’. *Geophysical Research Letters* **38**(L06102):1–4.
- D. A. Gurnett, et al. (2004). ‘The Cassini radio and plasma wave investigation’. *Space Science Reviews* **114**:395–463.
- R. M. Haberli, et al. (1996). ‘Heating of the thermal electrons in the comet of comet 1P/Halley’. *Journal of Geophysical Research* **101**(A7):15579–15589.
- R. Hajra, et al. (2017). ‘Dynamic unmagnetized plasma in the diamagnetic cavity around comet 67P/Churyumov–Gerasimenko’. *Monthly Notices of the Royal Astronomical Society* **475**:4140–4147.
- K. C. Hansen, et al. (2016). ‘Evolution of water production of 67P/Churyumov–Gerasimenko: An empirical model and a multi-instrument study’. *Monthly Notices of the Royal Astronomical Society* **462**(January 2018):S491–S506.
- L. Haser (1957). ‘Distribution d’intensité dans la tête d’une comète’. *Bulletin de la Societe Royale des Sciences de Liege* **43**:740–750.
- P. Henri, et al. (2017). ‘Diamagnetic region(s): structure of the unmagnetised plasma around Comet 67P/CG’. *Monthly Notices of the Royal Astronomical Society* **469**:S372–S379.
- K. L. Heritier, et al. (2017). ‘Vertical structure of the near-surface expanding ionosphere of comet 67P probed by Rosetta’. *Monthly Notices of the Royal Astronomical Society* **469**:S118–S129.
- T. W. Hill, et al. (2012). ‘Charged nanograins in the Enceladus plume’. *Journal of Geophysical Research* **117**(A05209):1–11.
- J. K. Hillier, et al. (2007). ‘The composition of Saturn’s E ring’. *Monthly*

- Notices of the Royal Astronomical Society* **377**:1588–1596.
- M. K. G. Holmberg (2013). *Licentiate Thesis*. Licentiate thesis, Uppsala University, IRFU.
- M. Horányi, et al. (2004). ‘Dusty plasma effects in Saturn’s magnetosphere’. *Reviews* **42**(RG4002):1–20.
- O. Ishihara (2007). ‘Complex plasma: dusts in plasma’. *Journal of Physics D: Applied Physics* **40**(8):R121–R147.
- Y. Itikawa & N. Mason (2005). ‘Cross sections for electron collisions with water molecules’. *Journal of Physical and Chemical Reference Data* **34**(1):1–22.
- Y.-D. Jia, et al. (2010). ‘Interaction of Saturn’s magnetosphere and its moons: 1. Interaction between corotating plasma and standard obstacles’. *Journal of Geophysical Research (Space Physics)* **115**:4214.
- G. Jones, et al. (2009). ‘Fine jet structure of electrically charged grains in Enceladus’ plume’. *Geophysical Research Letters* **36**(L16204):1–6.
- H. U. Keller, et al. (2015). ‘The changing rotation period of comet 67P/Churyumov-Gerasimenko controlled by its activity’. *Astronomy & Astrophysics* **579**:L5.
- S. Kellock, et al. (1996). ‘Cassini dual technique magnetometer instrument (MAG)’. In L. Horn (ed.), *Society of Photo-Optical Instrumentation Engineers (SPIE) Conference Series*, vol. 2803 of *Society of Photo-Optical Instrumentation Engineers (SPIE) Conference Series*, pp. 141–152. International Society for Optics and Photonics.
- S. Kempf, et al. (2008). ‘The E ring in the vicinity of Enceladus’. *Icarus* **193**:420–437.
- S. Kempf, et al. (2006). ‘The electrostatic potential of E ring particles’. *Planetary and Space Science* **54**:999–1006.
- C. Koenders, et al. (2015). ‘Dynamical features and spatial structures of the plasma interaction region of 67P/Churyumov-Gerasimenko and the solar wind’. *Planetary and Space Science* **105**:101–116.
- C. Koenders, et al. (2016). ‘Low-frequency waves at comet 67P/Churyumov-Gerasimenko Observations compared to numerical simulations’. *Astronomy & Astrophysics* **594**(A66):1–16.
- H. Kriegel, et al. (2014). ‘Ion densities and magnetic signatures of dust pickup at Enceladus’. *Journal of Geophysical Research: Space Physics* **119**(4):2740–2774.
- H. Kriegel, et al. (2011). ‘Influence of negatively charged plume grains on the structure of Enceladus’ Alfvén wings: Hybrid simulations versus Cassini Magnetometer data’. *Journal of Geophysical Research (Space Physics)* **116**(A10223):1–19.
- H. Kriegel, et al. (2009). ‘The plasma interaction of Enceladus: 3D hybrid

- simulations and comparison with Cassini MAG data'. *Planetary and Space Science* **57**:2113–2122.
- N. Krupp, et al. (2012). 'The Cassini Enceladus encounters 2005–2010 in the view of energetic electron measurements'. *Icarus* **218**:433–447.
- W. Kurth, et al. (2006). 'Cassini RPWS observations of dust in Saturn's E Ring'. *Planetary and Space Science* **54**:988–998.
- Y. Langevin, et al. (2016). 'Typology of dust particles collected by the COSIMA mass spectrometer in the inner coma of 67P/Churyumov Gerasimenko'. *Icarus* **271**:76–97.
- J. S. Leisner, G. B. Hospodarsky, & D. a. Gurnett (2013). 'Enceladus auroral hiss observations: Implications for electron beam locations'. *Journal of Geophysical Research: Space Physics* **118**(1):160–166.
- K. E. Mandt, et al. (2016). 'RPC observation of the development and evolution of plasma interaction boundaries at 67P/Churyumov-Gerasimenko'. *Monthly Notices of the Royal Astronomical Society* **462**:S9–S22.
- M. Massironi, et al. (2015). 'Two independent and primitive envelopes of the bilobate nucleus of comet 67P'. *Nature* **526**:402–405.
- K. J. Meech (2017). 'Setting the scene: what did we know before Rosetta?'. *Philosophical Transactions A* **375**:1–19.
- R. L. Merlino (2006). 'Dusty plasmas and applications in space and industry'. In C. Grabbe (ed.), *Plasma Physics Applied*, chap. 5, pp. 73–110. Transworld Research Network.
- S. Merouane, et al. (2016). 'Dust particle flux and size distribution in the coma of 67P/Churyumov-Gerasimenko measured in situ by the COSIMA instrument on board Rosetta'. *Astronomy & Astrophysics* **596**:A87.
- M. Morooka, et al. (2011). 'Dusty plasma in the vicinity of Enceladus'. *Journal of Geophysical Research (Space Physics)* **116**(A12221):1–15.
- H. Mott-Smith & I. Langmuir (1926). 'The Theory of Collectors in Gaseous Discharges'. *Physical Review* **28**:727–763.
- S. Mottola, et al. (2014). 'The rotation state of 67P/Churyumov-Gerasimenko from approach observations with the OSIRIS cameras on Rosetta'. *Astronomy and Astrophysics* **569**(L2):1–5.
- NASA - JPL (2012). 'Cassini Solstice Mission'. World wide web: [\url{http://saturn.jpl.nasa.gov/}](http://saturn.jpl.nasa.gov/).
- F. Neubauer (1980). 'Nonlinear standing Alfvén wave current system at Io: Theory'. *Journal of Geophysical Research* **85**(A3):1171–1178.
- H. Nilsson, et al. (2007). 'RPC-ICA: The ion composition analyzer of the Rosetta plasma consortium'. *Space Science Reviews* **128**:671–695.

- E. Odelstad, et al. (2015). 'Evolution of the plasma environment of comet 67P from spacecraft potential measurements by the Rosetta Langmuir probe instrument'. *Geophysical Research Letters* **42**(23):10,126–10,134.
- E. Odelstad, et al. (2017). 'Measurements of the electrostatic potential of Rosetta at comet 67P'. *Monthly Notices of the Royal Astronomical Society* **469**:S568–S581.
- J. Olson, et al. (2010). 'On the interpretation of Langmuir probe data inside a spacecraft sheath.'. *The Review of scientific instruments* **81**(105106):1–8.
- N. Omidi, et al. (2010). 'Hybrid Simulations of Plasma-Neutral-Dust Interactions at Enceladus'. In *Proceedings of the 9th Annual International Astrophysics Conference*, vol. 1302, pp. 237–242. AIP Publishing.
- N. Omidi, et al. (2012). 'Flow stagnation at Enceladus: The effects of neutral gas and charged dust'. *Journal of Geophysical Research* **117**(A06230):1–15.
- E. Pailharey & F. Vignaux (2004). 'Cassini Huygens - A Probe to Titan'. ESA Publications Division, ESTEC.
- M. Pätzold, et al. (2016). 'A homogeneous nucleus for comet 67P/Churyumov-Gerasimenko from its gravity field'. *Nature* **530**(7588):63–65.
- A. Pedersen (1995). 'Solar wind and magnetosphere plasma diagnostics by spacecraft electrostatic potential measurements'. *Annales Geophysicae* **13**:118–129.
- A. Pedersen, F. Mozer, & G. Gustafsson (1998). 'Electric Field Measurements in a Tenuous Plasma with Spherical Double Probes'. *Measurement Techniques in Space Plasmas – Fields: Geophysical Monograph 103*. Edited by Robert F. Pfaff.
- D. H. Pontius & T. W. Hill (2006). 'Enceladus: A significant plasma source for Saturn's magnetosphere'. *Journal of Geophysical Research: Space Physics* **111**(A09214):1–8.
- C. C. Porco, et al. (2006). 'Cassini Observes the Active South Pole of Enceladus'. *Science* **311**:1393–1401.
- Preusker, F., et al. (2017). 'The global meter-level shape model of comet 67p/churyumov-gerasimenko'. *Astronomy & Astrophysics* **607**:L1.
- W. R. Pryor, et al. (2011). 'The auroral footprint of Enceladus on Saturn.'. *Nature* **472**:331–333.
- I. Richter, et al. (2015). 'Observation of a new type of low-frequency waves at comet 67P/Churyumov-Gerasimenko'. *Annales Geophysicae* **33**(8):1031–1036.
- A. Rotundi, et al. (2015). 'Dust measurements in the coma of comet 67P/Churyumov-Gerasimenko inbound to the Sun'. *Science* **347**(6220):1–6.



- A. Rotundi, et al. (2015). ‘Dust measurements in the coma of comet 67P/Churyumov-Gerasimenko inbound to the Sun’. *Science* **347**(1):aaa3905.
- J. Saur, F. M. Neubauer, & N. Schilling (2007). ‘Hemisphere coupling in Enceladus’ asymmetric plasma interaction’. *Journal of Geophysical Research* **112**(A11209):1–11.
- M. Shafiq, et al. (2011). ‘Characteristics of the dust-plasma interaction near Enceladus’ South Pole’. *Planetary and Space Science* **59**:17–25.
- P. K. Shukla (2001). ‘A survey of dusty plasma physics’. *Physics of Plasmas* **8**:1791–1803.
- S. Simon, et al. (2011). ‘Influence of negatively charged plume grains and hemisphere coupling currents on the structure of Enceladus’ Alfvén wings: Analytical modeling of Cassini magnetometer observations’. *Journal of Geophysical Research* **116**(A04221):1–33.
- S. Simon, et al. (2014). ‘Discontinuities in the magnetic field near Enceladus’. *Geophysical Research Letters* **41**:1–8.
- C. Simon Wedlund, et al. (2016). ‘The atmosphere of comet 67p/churyumov-gerasimenko diagnosed by charge-exchanged solar wind alpha particles’. *Astronomy & Astrophysics* **587**:A154.
- F. Spahn, et al. (2006a). ‘E ring dust sources: Implications from Cassini’s dust measurements’. *Planetary and Space Science* **54**(9–10):1024–1032.
- F. Spahn, et al. (2006b). ‘Cassini dust measurements at Enceladus and implications for the origin of the E ring.’. *Science* **311**:1416–1418.
- J. Spitale & C. Porco (2007). ‘Association of the jets of Enceladus with the warmest regions on its south-polar fractures’. *Nature* **449**(11):695–697.
- G. Stenberg Wieser, et al. (2017). ‘Investigating short-time-scale variations in cometary ions around comet 67P’. *Monthly Notices of the Royal Astronomical Society* **469**:S522–S534.
- M. Taylor, et al. (2017). ‘The Rosetta mission orbiter Science overview – the comet phase’. *Philosophical Transactions A* **375**:1–20.
- V. Tenishev, M. Combi, & B. Davidsson (2008). ‘A Global Kinetic Model for Cometary Comae: The Evolution of the Coma of the Rosetta Target Comet Churyumov-Gerasimenko throughout the Mission’. *The Astrophysical Journal* **685**:659–677.
- P. Thomas, et al. (2007). ‘Shapes of the saturnian icy satellites and their significance’. *Icarus* **190**(2):573 – 584. Deep Impact Mission to Comet 9P/Tempel 1, Part 2.
- R. L. Tokar, et al. (2006). ‘The Interaction of the Atmosphere of Ence-

- ladus with Saturn's Plasma'. *Science* **311**:1409–1412.
- R. L. Tokar, et al. (2008). 'Cassini detection of water-group pick-up ions in the Enceladus torus'. *Geophysical Research Letters* **35**(L14202):1–5.
- J. G. Trotignon, et al. (2007). 'RPC-MIP : The Mutual Impedance Probe of the Rosetta Plasma Consortium'. *Space Science Reviews* **128**:713–728.
- C.-y. Tzou (2017). *Calibrations of ROSINA-COPS and Observations at Comet*. Ph.D. thesis, University Bern.
- E. Vigren, et al. (2016). 'Model-Observation Comparison of Electron Number Densities in the Coma of 67P/Churyumov-Gerasimenko During 2015 January'. *The Astronomical Journal* **152**(59):1–8.
- E. Vigren & A. I. Eriksson (2017). 'A 1d model of radial ion motion interrupted by ion-neutral interactions in a cometary coma'. *The Astronomical Journal* **153**(4):150.
- E. Vigren & M. Galand (2013). 'Predictions of Ion Production Rates and Ion Number Densities within the Diamagnetic Cavity of Comet 67P/Churyumov-Gerasimenko at Perihelion'. *Astrophysical Journal* **772**:33.
- J.-E. Wahlund, et al. (2009). 'Detection of dusty plasma near the E-ring of Saturn'. *Planetary and Space Science* **57**:1795–1806.
- J.-E. Wahlund, et al. (2005). 'The inner magnetosphere of Saturn: Cassini RPWS cold plasma results from the first encounter'. *Geophysical Research Letters* **32**(L20S09):1–4.
- J. H. Waite, et al. (2006). 'Cassini ion and neutral mass spectrometer: Enceladus plume composition and structure.'. *Science (New York, N.Y.)* **311**:1419–1422.
- Z. Wang (2006). *The Characteristics of Dust Particles Detected by Cassini Near Saturn's Ring Plane*. Doctorate, University of Iowa.
- Z. Wang, et al. (2006). 'Characteristics of dust particles detected near Saturn's ring plane with the Cassini Radio and Plasma Wave instrument'. *Planetary and Space Science* **54**:957–966.
- L. Yang, et al. (2016). 'Observations of high-plasma density region in the inner coma of 67p/churyumov-gerasimenko during early activity'. *Monthly Notices of the Royal Astronomical Society* **462**:S33–S44.



# Acta Universitatis Upsaliensis

*Digital Comprehensive Summaries of Uppsala Dissertations  
from the Faculty of Science and Technology 1673*

Editor: The Dean of the Faculty of Science and Technology

A doctoral dissertation from the Faculty of Science and Technology, Uppsala University, is usually a summary of a number of papers. A few copies of the complete dissertation are kept at major Swedish research libraries, while the summary alone is distributed internationally through the series Digital Comprehensive Summaries of Uppsala Dissertations from the Faculty of Science and Technology. (Prior to January, 2005, the series was published under the title "Comprehensive Summaries of Uppsala Dissertations from the Faculty of Science and Technology".)



ACTA  
UNIVERSITATIS  
UPSALIENSIS  
UPPSALA  
2018

Distribution: [publications.uu.se](http://publications.uu.se)  
urn:nbn:se:uu:diva-348856